ACS OMEGA

http://pubs.acs.org/journal/acsodf

Article

Construction of Pyrazine-Appended 1D and 3D Cobalt(II) Succinate Coordination Polymers: Influence of Solvent on Architectures and Applications in Gas Adsorption and NAC Detection

Luann R. D'souza, Nikita N. Harmalkar, Sarvesh S. Harmalkar, Sakharam B. Tayade, and Sunder N. Dhuri*

Cite This: *ACS Omega* 2022, 7, 5698−5712

Read Online

ACCESS | Metrics & More | Article Recommendations | Supporting Information

ABSTRACT: An underexplored reaction of pyrazine (rigid and linear) and succinic acid (flexible) with $Co(NO_3)_2{\cdot}6H_2O$ afforded four new coordination polymers (CPs): $[Co(H_2O)(pyz)(suc)]$ (**1**), $[Co(H_2O)_2(pyz)(suc)]$ (**2**), $[Co(H_2O)_4(pyz)](suc)$ (**3**) and $[Co_2(H_2O)_2(pyz)(suc)_2]$ (**4**), as well as $[Co(HCO_2)_2(pyz)]$ (**5**) being lately reported along with well-known **6** and **7**. The CPs were obtained as stable crystalline materials and characterized by conventional solid-state techniques, including X-ray crystallography. Hydrothermally produced compounds **1** and **2** were both 3D CPs. While **3** and **4** obtained under ambient/solvothermal conditions in DMSO generated 1D and 3D structures, **5** isolated from DMF under solvothermal conditions had a 3D structure. The topologies of the coordination polymers **1**−**7** were described by underlying nets 3D 5-c **fet**, 3D 4-c **cds**, 1D 2-c **2C1**, 3D 5-c **bnn**, 3D 6-c **rob**, 1D 2-c **2C1**, and 3D 6-c **pcu**, respectively. The plot of χ_M^{-1} versus T was essentially linear in the entire temperature range following the Curie−Weiss law with a Curie constant (C) of 2.525 and a negative Weiss constant (ϕ) of −46.24 K, suggesting weak antiferromagnetic (AF) exchange interactions. CO_2 and N_2 adsorption studies of **1**−**5** featured type III isotherms. **1** was found to show remarkably higher quenching efficiencies for nitrophenols (η = 98% for *o*-NP) over other NACs. The Stern−Volmer plot exhibited deviation in linearity with K_{sv} values about 200 times greater than that for the simplest nitroaromatic compound (NB), signifying its exclusive quenching ability toward **1**. The LOD for *p*-NP addition to **1** was found to be 0.995 ppm.

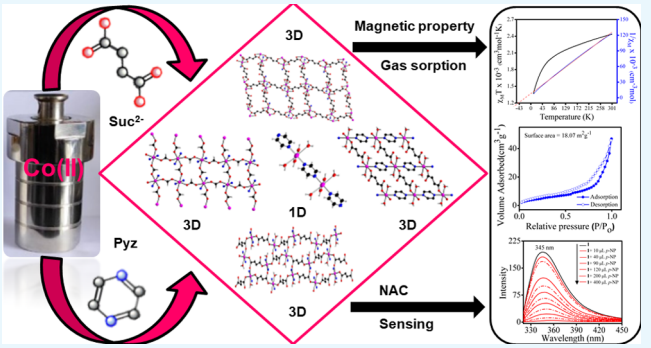

INTRODUCTION

Coordination polymers and metal−organic frameworks (MOFs) form an interdisciplinary area of research with MOFs endorsing high porosity, thermal stability, robustness, tunable metrics, and organic functionality, resulting in intriguing structural diversities.[1−4] The sewing of molecular building units by strong bonds into predetermined extended structures alongside weak noncovalent interactions (hydrogen-bonding, $\pi-\pi$ stacking, and van der Waals forces) generates supramolecular assemblies.[5−9] These play promising roles in applications such as catalysis,[10−12] chemical adsorption,[13,14] gas adsorption,[15−19] and magnetism.[20−24] Hydro(solvo)-thermal conditions alongside the compositional and process parameters assist the formation of M−O−M extensions having a profound effect on the overall structure and stability.[25−30] The employment of mixed ligands favors frameworks with diverse structural motifs, in comparison to using only one type of ligands. Flexible dicarboxylates in combination with linear rodlike ligands mediate the construction of coordination polymers (CPs) ranging from 1D to 3D networks. Hence, the ligands chosen, i.e., succinic acid and pyrazine, serve as suitable candidates. Succinic acid is flexible containing two carboxylate groups in 1,4-positions adopting monodentate, bridging, and bridging chelate coordination modes to the metal as seen in our work, while pyrazine is a rigid-planar bidentate diimine ligating through the μ_2 bridging mode. There is growing recognition for such systems in the field of molecular magnetism as they act as antiferromagnetic (AF) couplers in transition-metal complexes.

With industrialization, there has been exploitation of organic dyes, nitroaromatic compounds (NACs), causing a serious threat to the environment and health. This has triggered the development of fluorescent sensor materials for the selective and judicious detection of organic dyes and removal of harmful

Received: September 20, 2021
Accepted: January 21, 2022
Published: February 10, 2022

Table 1. Crystal Data and Structure Refinement Parameters for 1−4

empirical formula	$C_8H_{10}CoN_2O_5$	$C_8H_{12}CoN_2O_6$	$C_4H_{16}CoN_2O_8$	$C_{12}H_{16}Co_2N_2O_{10}$
	1	**2**	**3**	**4**
formula weight (g mol^{-1})	273.11	291.13	327.16	466.13
temperature (K)	296(2)			
wavelength (Å)	0.71073			
crystal system	monoclinic	monoclinic	orthorhombic	triclinic
space group	$P21/c$	$C2/c$	$Pnnm$	$P\bar{1}$
a (Å)	7.1468(2)	12.7414(5)	10.316(4)	7.7368(4)
b (Å)	17.7533(6)	6.7729(2)	7.114(3)	9.0843(5)
c (Å)	8.5534(2)	13.4227(4)	9.458(4)	11.321(6)
α (deg)	90	90	90	90.118(1)
β (deg)	103.3180(1)	107.6590(1)	90	99.312(1)
γ (deg)	90	90	90	97.756(1)
volume ($Å^3$)	1056.06(5)	1103.75(6)	694.1(5)	777.78(7)
Z	4	4	2	2
calcd density (mg m^{-3})	1.718	1.752	1.565	1.99
absorption coefficient (mm^{-1})	1.632	1.574	1.271	2.194
$F(000)$	556	596	338	472
diffractometer	Bruker D8 Quest Eco			
theta range for data collection (deg)	2.703−28.302	3.185−28.283	2.922−28.319	2.872−28.264
completeness to theta	98.4	99.7	100	100
index ranges	$-8 \le h \le 9$	$-16 \le h \le 14$	$-13 \le h \le 13$	$-10 \le h \le 10$
	$-21 \le k \le 23$	$-9 \le k \le 8$	$-9 \le k \le 9$	$-12 \le k \le 12$
	$-11 \le l \le 9$	$-17 \le l \le 17$	$-12 \le l \le 12$	$-15 \le l \le 15$
reflections collected	10 816	8722	8915	11 979
independent reflections	2586 (R_{int} = 0.0314)	1364 (R_{int} = 0.049)	924 (R_{int} = 0.0326)	3853 (R_{int} = 0.0315)
refinement method	full-matrix least-squares on F^2			
absorption correction	semiempirical from equivalents			
data/restraints/parameters	2586/0/151	1364/0/85	924/0/56	3845/0/247
goodness-of-fit on F^2	1.063	1.066	1.196	1.054
final R indices [I > 2sigma(I)]	R_1 = 0.0281, wR_2 = 0.0629	R_1 = 0.0294, wR_2 = 0.0676	R_1 = 0.0357, wR_2 = 0.0793	R_1 = 0.0309, wR_2 = 0.0664
R indices (all data)	R_1 = 0.0389, wR_2 = 0.0693	R_1 = 0.0472, wR_2 = 0.0772	R_1 = 0.0422, wR_2 = 0.083	R_1 = 0.0449, wR_2 = 0.0737
largest diff. peak and hole (e $Å^{-3}$)	0.516, −0.424	0.317, −0.425	0.573, −0.451	0.472, −0.541
CCDC number	2098543	2098544	2098545	2098548

substances. One promising approach toward NAC detection is the use of fluorescent electron-rich MOFs undergoing quenching on interaction with electron-deficient nitroaromatic molecules. Fluorescence sensing is a promising strategy to tackle the detection of nitro explosives owing to its low cost, electronic tunability, portability, and easy operation.[31−37] To the best of our knowledge, the MOFs with succinate and pyrazine linkers together have not been explored, and only the coordination polymer $[Cd_2(H_2O)_2(pyz)(suc)_2]$ has been reported.[38] In addition to this, compounds $[Co(HCOO)_2(pyz)]$ **5** and $[Co(H_2O)_4(suc)]$ **6** are well-known.[39,40] Hence, bearing in mind the less explored chemistry of cobalt(II) with succinate and pyrazine, we have attempted the synthesis of five cobalt(II) coordination polymers by tuning the synthetic conditions and the solvent. On our way to prepare compounds **1**−**5**, we obtained **6** and **7** as secondary products. We investigated the gas sorption ability of the compounds for N_2 and CO_2 gases. In addition, we have tested **1** for its selective detection of nitroaromatic compounds (NACs).

RESULTS AND DISCUSSION

Structural Description. *Single-Crystal Structure Determination.* The single crystals of **1**−**7** were determined using a Bruker D8 Quest Eco X-ray diffractometer at 296 K, equipped with Mo Kα (λ = 0.71073 Å) radiation. The program suite APEX3 (version 2018.1) was used to integrate the frames, perform absorption correction, and determine the unit cell. The structures were solved with SHELXS, and subsequent refinements on F^2 using full-matrix least-squares methods were performed with SHELXL.[41] The refinement of nonhydrogen atoms was performed in an anisotropic manner, while the hydrogen atoms were located at calculated positions.

*[Co(H_2O)(pyz)(suc)] (**1**).* X-ray analysis of **1** revealed its crystallization in the monoclinic $P21/c$ space group (Table 1). The asymmetric unit consists of one Co(II), one pyz, one suc^{2-}, and one water molecule. Three oxygen atoms from each succinate ligand (O1, $O3^{i}$, $O4^{ii}$), one water molecule (O5w), and two nitrogen atoms from the bridging pyrazine (N1 and $N2^{iii}$) complete the octahedral coordination of Co(II) (Figure 1). The typical Co−O bond length varies from 2.061 to 2.101 Å, with Co−N distances ranging 2.169−2.188 Å, and that for Co−O5w is 2.083 Å (Table S1), which clearly indicates distortion from the ideal octahedral geometry. These measures are comparable to Co(II) compounds containing succinate or pyrazine (Table S2).[8,42−46] The oxygen atoms of succinate adopt monodentate coordination to cobalt i.e., one oxygen atom coordinated to cobalt (κ-O) (**mode I** depicted in Table 2). The succinate ligands adopt anti−anti conformation with torsion angle χ[C(1)C(2)C(3)C(4)] = −168.62°. The

https://doi.org/10.1021/acsomega.1c05216
ACS Omega 2022, 7, 5698−5712

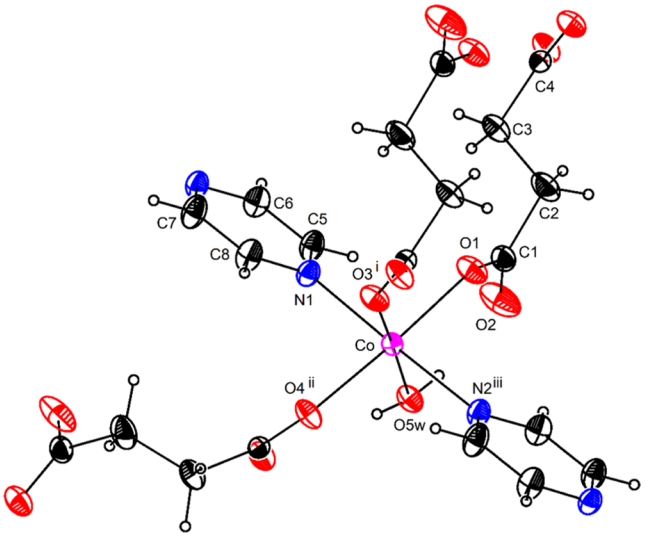

Figure 1. Crystal structure of $[Co(H_2O)(pyz)(suc)]$ **1**, showing the thermal ellipsoids drawn at the 50% probability level for all of the atoms except for the H atoms that are shown as spheres of arbitrary radii. Symmetry code: (i) $-x + 1, -y + 1, -z + 1$; (ii) $-x + 1, y + 1/2, -z + 3/2$; and (iii) $x + 1, y, z$.

orientation of carboxylate with respect to the backbone line of succinate generates angles [O(1)C(1)C(2)], [O(4)C(4)-C(3)], and [O(3)C(4)C(3)] equal to 116.63, 117.86, and 119.37°, respectively.[38,47] Pyrazine ligates cobalt via κ-N mode.[38,48−54] On viewing **1** along the *c* direction, pyz forms a bridge between the cobalt centers with an intrachain Co···Co separation distance of 7.147(0) Å (Figure 2). While on perceiving **1** in the *a*-axis (Figure S1), two rings are seen: a 14-membered ring built from two cobalt centers [Co(a) and Co(b)] stitched in a *cis* fashion by sharing two succinate oxygen atoms (O1 and $O3^i$) in the *bis*-monodentate mode and a larger 22-membered ring composed of four cobalt centers [Co(b) and Co(e)] connected by $O4^{ii}$ and O1 of succinate in the *bis*-monodentate fashion and Co(c) and Co(d) linked via O1 and $O4^{ii}$ of succinate in the same mode. On observing the ring structures, it can be seen that the water molecules lie within the bigger ring, while they are disposed of outside the 14-membered ring. The Co···Co separation distance in the smaller ring is 7.275(1) Å, while that in the larger ring is

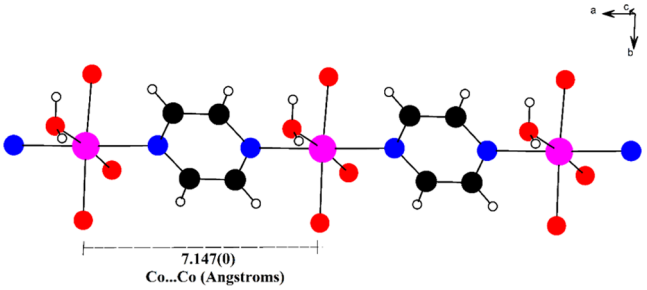

Figure 2. View of **1** showing extension of pyrazine along the *c*-axis.

12.412(1) Å. The molecular packing of **1** viewed along the *a**-axis displays a 3D array (Figure S2).

To understand the coordination modes of the ligands forming the framework, we performed a topological analysis of **1**.[55] The succinate ligand bridges three cobalt centers by involving three oxygen donor atoms. Following the notation of the coordination mode for succinate anion as T^3, the overall coordination formula of **1** is $AT^3B^2M^1$. The underlying net of **1** is 3,5-c fet due to succinate that coordinates three Co atoms (hence 3-c) and 5-c Co atoms that connect two pyrazine and three succinate molecules (Table 3).[56−58] The hydrogen-bonding interactions of **1** are summarized in Table S3.

*$[Co(H_2O)_2(pyz)(suc)]$ (**2**).* It crystallizes in the monoclinic *C*2/*c* space group (Table 1). The asymmetric unit is composed of two oxygen atoms (O2 and $O2^i$) of succinate, two nitrogen atoms from two different pyrazine ligands (N1 and $N1^i$), and two water molecules (O1w and $O1w^i$) (Figure 3). Succinate also adopts monodentate coordination to cobalt, i.e., one oxygen atom coordinated to cobalt (κ-O) and one pyz ligated cobalt via κ-N mode, as seen in **1**. The typical Co−O, Co−N, and Co−O1w bond distances measure 2.064, 2.207, and 2.111 Å, respectively (Table S1), lying in accordance with **1** and reported cobalt(II) compounds containing succinate or pyrazine (Table S2).[8,42−46] The succinate ligands adopt gauche conformation with torsion angle χ[C(3)C(4)C(4′)-C(3′)] = −59.41°, and the orientation of the carboxylate groups with respect to the C−C backbone of succinate generates angle [O(2)C(3)C(4)] = 116.71°. The intrachain Co···Co separation distance through bridging pyz is 7.215(0) Å, and that bridged by succinate is 7.726(5) Å (Figure S3a,b).[38,47−54] The propagation of **2** in the *b* direction through succinate results in the formation of rectangular grids of

Table 2. Observed Coordination Modes for Succinate in 1−6

Sr. No.	Oxygen atoms of suc^{2-} coordinating	Coordination mode to Co
1	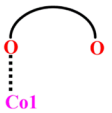	**Mode I:** Monodentate κ-*O* seen in **1**, **2** and **6**.
2	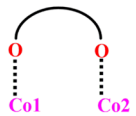	**Mode II:** Bridging κ-O for Co1 and Co2 seen in **4**.
3	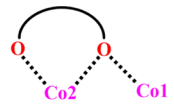	**Mode III:** Bridging chelate κ^2-*O, O′* and κ-*O* seen in **4**.

https://doi.org/10.1021/acsomega.1c05216
ACS Omega 2022, 7, 5698−5712

Table 3. Coordination Formulae and Net Representations for 1−6

compound	chemical formula	space group	dimension	coordination formula	ligand composition	observed net
1	$C_8CoH_{10}N_2O_5$	*P*21/*c*	3D	$AT^3B^2M^1$	$H_2O[M^1]$ $C_4H_4O_4[T^3]$ $C_4H_4N_2[B^2]$	fet
2	$C_8CoH_{12}N_2O_6$	*C*2/*c*	3D	$AB_2^2M_2^1$	$C_4H_4N_2[B^2]$ $H_2O[M^1]$ $C_4H_4O_4[B^2]$	cds
3	$C_8CoH_{14}N_2O_8$	*Pnnm*	1D	$AB^2M_4^1$	$C_4H_4N_2[B^2]$ $H_2O[M^1]$ $C_4H_4O_4$ [0D-not coordinated]	linear chain
4	$C_6CoH_8NO_5$	$P\bar{1}$	3D	$A_4K^{22}K^4T_2^{11}B_2^2M_4^1$	$C_4H_4N_2[B^2]$ $H_2O[M^1]$ $C_4H_4O_4[K^4]$ $C_4H_4O_4[K^{22}]$ $C_4H_4O_4[T^{11}]$	twofold bnn
5	$C_6CoH_6N_2O_4$	*C*2/*c*	3D	AB_3^2	$C_4H_4N_2[B^2]$ $CHO_2[B^2]$	rob
6	$C_4CoH_{12}O_8$	*P*21/*c*	1D	$AB^2M_4^1$	$H_2O[M^1]$ $C_4H_4O_4[B^2]$	linear chain

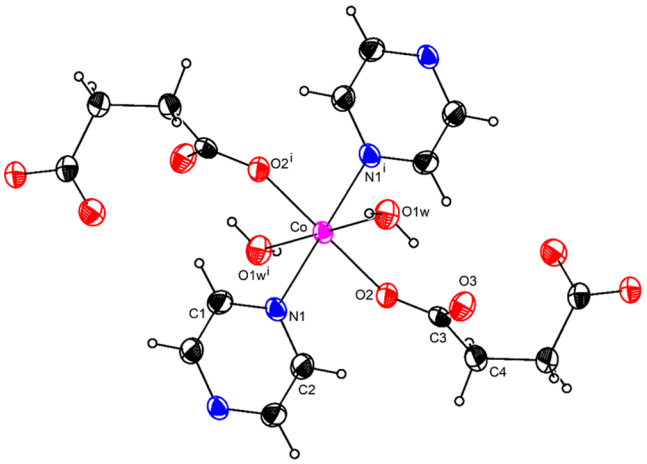

Figure 3. Crystal structure of $[Co(H_2O)_2(pyz)(suc)]$ (**2**), showing the thermal ellipsoids drawn at the 50% probability level for all of the atoms except for the H atoms that are shown as spheres of arbitrary radii. Symmetry code: (i) $-x + 3/2, -y + 3/2, -z + 1$.

7.215(0) × 7.726(5) Å dimensions (Figure 4). Topological study of **2** reveals succinate bridging of two cobalt centers in

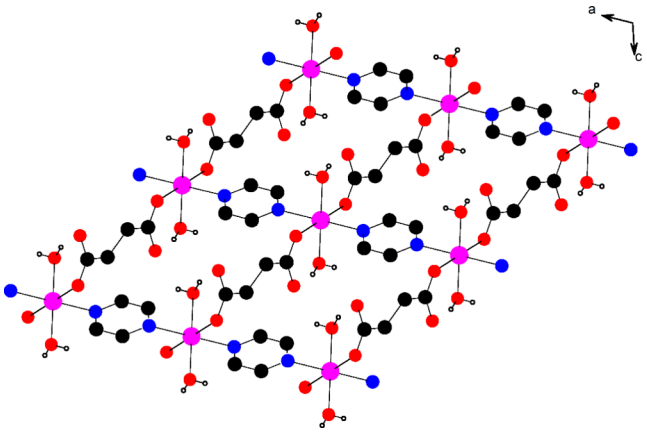

Figure 4. Packing diagram of **2** viewed along the *b* direction displaying rectangular channels formed between interlayered pyrazine bridges.

the *bis*-monodentate fashion by coordination of two oxygen atoms of one succinate linking to two cobalt atoms. Hence, the coordination mode for succinate is B (two donor oxygen atoms used in total), and since $m = 2$, it becomes B^2. On the other hand, pyrazine adopts coordination mode B^2* since it uses two donor atoms (N atoms) for coordination and connects to two cobalt atoms via one donor atom each ($m = 2$). Finally, two terminal water molecules have coordination mode M^1 as each water molecule possesses one donor atom and coordinates one cobalt atom ($m = 1$). The coordination formula of **2** is represented as $AB^2B^2M^1$.[55] The topological analysis of **2** resulted in the 4-connected underlying net **cds** with both pyrazine and succinate 2-c bridged (Table 3).[56,59] The subnets {Co(pyz)} and {Co(suc)} are represented by 2-c simple chains intersecting at the Co atoms. The hydrogen-bonding interactions in **2** are shown in Table S3.

*$[Co(H_2O)_4(pyz)_2](suc)$ (**3**).* On switching the reaction in DMSO under room temperature conditions, bright orange crystalline plates of **3** were obtained, which crystallized in the orthorhombic *Pnnm* space group (Table 1). The crystal structure shows cobalt coordinated to two nitrogen atoms of pyz (N1 and $N1^{iii}$), four oxygen atoms of water (O1w, $O1w^{i-iii}$), and an uncoordinated succinate dianion (Figure 5).

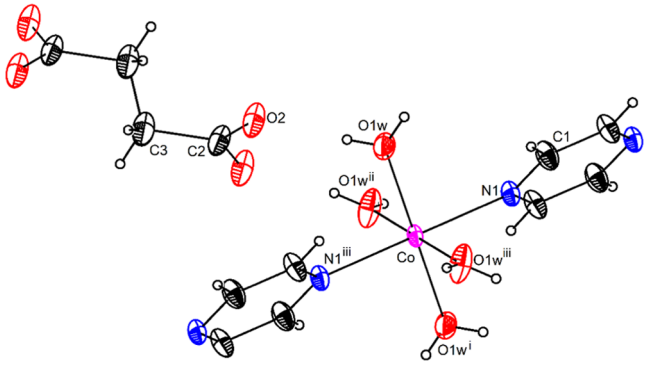

Figure 5. Crystal structure of $[Co(H_2O)_4(pyz)](suc)$ (**3**) showing the thermal ellipsoids drawn at the 50% probability level for all of the atoms except for the H atoms that are shown as spheres of arbitrary radii. Symmetry code: (i) $-x + 1, -y + 1, -z + 1$ (ii) $x, y, -z + 1$ (iii) $-x + 1, -y + 1, z$.

The uncoordinated succinate plays a templating as well as charge compensating role and adopts *anti* conformation with torsion angle $\chi[C(2)C(3)C(3')C(2')] = 180°$, and the orientation of the carboxylate with respect to the succinate backbone is $[O(2)C(2)C(3)] = 117.54°$.[38,47] The Co−N distance of 2.166(2) Å in **3** is consistent with the reported $[CoCl_2(pyz)_2]_n$ and $[CoCl_2(pyz)]_n$ compounds (Table S2), where one pyz ligates one cobalt atom in the κ-N mode.[60−65] The cobalt centers are terminated (M^1 mode) by four water molecules and bridged (B^2 mode) via pyz with a Co···Co spacing of 7.114 Å to form coordination formula $AB^2M_4^1$.[55] This coordination mode results in topology **2C1** for simple 2-c linear chains (Table 3 and Figure S4).[56] The uncoordinated succinate anions connect the coordination chains into 3D supramolecular architecture through H-bonds with coordinated water molecules.

*$[Co_2(H_2O)_2(pyz)(suc)_2]$ (**4**).* Subjecting the reaction under solvothermal conditions in DMSO gave purple crystalline

https://doi.org/10.1021/acsomega.1c05216
ACS Omega 2022, 7, 5698−5712

cubes of **4** crystallizing in the triclinic $P\bar{1}$ space group (Table 1). The crystal structure is composed of succinate oxygen atoms (O2 and O3) adopting bridging coordination to Co1 and Co2, respectively (**mode II**, Table 2), while O4 and O5 of succinate coordinate Co1 and Co2 via bridging the chelate (**mode III**, Table 2). In total, four carboxylate oxygen atoms of three different succinate ligands coordinate a single cobalt ion (κ^4-*O*,*O*′,*O*″,*O*‴ mode), while one pyz ligates per cobalt via the κ-N mode (Figure 6).[8,38,48−54] The Co1−O bond distances

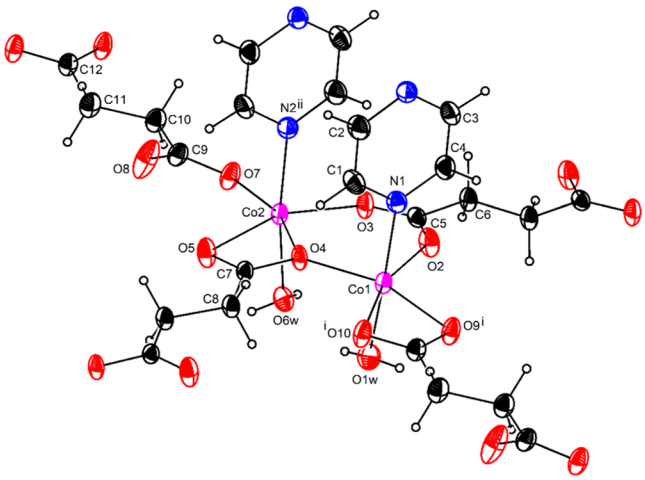

Figure 6. Crystal structure of $[Co_2(H_2O)_2(pyz)(suc)_2]$ (**4**) showing the thermal ellipsoids drawn at the 50% probability level for all of the atoms except for the H atoms that are shown as spheres of arbitrary radii. Symmetry code: (i) $x - 1, y + 1, z$ (ii) $-x, -y + 1, -z + 1$.

range from 2.0154(17) to 2.2137(17) Å, while that of Co1−N1 is 2.164(2) Å. However, the bond distances for Co2−O lie between 1.9956(16) and 2.2786(17) Å and that for Co2−N2 is 2.179(2) Å (Table S1). The view of **4** along the *a*-axis shows succinate extending between two cobalt centers with the Co1···Co2 separation distance of 3.625(0) Å, and the distance bridged by pyz is 7.133(5) Å (Figure S5a). The succinate ligands adopt the anti−anti conformation with torsion angles χ[C(12)C(11)C(10)C(9)], χ[C(7)C(8)C(8′)C(7′)], and χ-[C(5)C(6)C(6′)C(5′)] equal to 172.4, −180, and 180°, respectively (Figure S5b). The orientation of the carboxylate groups with respect to the C−C backbone of succinate generates angles [O(2)C(5)C(6)], [O(3)C(5)C(6)], [O(4)-C(7)C(8)], [O(5)C(7)C(8)], [O(7)C(9)C(10)], [O(9)-C(12)C(11)], and [O(10)C(12)C(11)] equal to 117.3, 116.8, 118.68, 124, 115.02, 120.89, and 119.39°, respectively.[38,47] The four or three donor atoms of the succinate anion participating in the formation of coordination bonds give coordination modes K^{22} and K^4 or T^{11}, respectively. Pyrazine adopts the B^2 mode using two donor atoms to coordinate two Co1 or two Co2. The terminal water molecules have coordination mode M^1 since each water molecule possesses one donor atom and is coordinated to Co1 or Co2. Therefore, the coordination formula of **4** is represented as $A_4K^{22}K^4T_2{}^{11}B_2{}^2M_4{}^1$. The succinate forms the {Co(suc)} subnet with 2D 4-c sql net topology and the layers are interconnected in an alternate fashion by pyrazine ligands into two interpenetrating frameworks. A pair of carboxylate groups from the succinate anion connect pairs of Co atoms into dimeric cluster $\{Co_2(COO)_2\}$. This cluster can be simplified into a five-coordinated node: four edges incident to the node are formed by four succinate anions, and one edge is formed by a pair of pyrazine molecules. The underlying net is therefore five-coordinated **bnn** with the dimeric cluster as the node (Table 3 and Figure S6).[55,56] The hydrogen-bonding interactions prevailing in **4** are shown in Table S3.

Very recently reported is $[Co(HCO_2)_2pyz]$ (**5**) by Sahoo and co-workers.[39] They have described the synthesis of $[Co(HCOO)_2(C_4H_4N_2)]$ (**5**) in DMF under solvothermal conditions using $Co(NO_3)_2{\cdot}6H_2O$ and pyrazine (1:2). The crystal structure was determined at 298 K and crystallizes in the monoclinic *C*2/*c* space group. Both the formate anion and pyz molecule exhibit the B^2 mode of coordination to complete the coordination formula $AB_3{}^2$ (Table 3).[55,56] This coordination formula results in the formation of a 3D framework from undulated sublayers $\{Co(HCO_2)_2\}$ bridged by pyrazine molecules in two directions [1$\bar{1}$0] and [110]. The underlying topology of the framework is described by 6-c net **rob** with pyrazine and formate both 2-c bridged. It is curious that a very similar topology has been described for $[Cd(CN)_2(pyz)]$.[66] The compound has been characterized by FTIR, TGA−DSC, high-resolution XPS, PXRD, FESEM, TEM analysis, and various temperature-dependent magnetic measurements. The compound shows in situ transformation owing to hydrolysis of DMF under high-temperature and basic conditions. On investigating the electrochemical catalytic performance of the compound, its promising role as an efficient electrocatalyst for the oxygen evolution reaction (OER) in alkaline media is revealed, thereby serving potential roles in applications for energy storage and conservation. In our work, we attempted to study the effect of solvent (DMF) in the reaction between $Co(NO_3)_2{\cdot}6H_2O$, disodium succinate, and pyrazine under solvothermal conditions. We anticipated the compound to contain succinate and pyrazine with enhanced dimensionality or nuclearity. However, to our utter surprise, we obtained the compound reported by Sahoo et al., incorporating the hydrolysis product of DMF. We determined its crystal structure and found that it crystallized in the monoclinic *C*2/*c* space group (Table S4) with cobalt surrounded by four oxygen atoms of formate (O1, $O2^{i-iii}$) and two nitrogen atoms of two pyz (N1 and $N1^{ii}$) (Figure 7). The Co−N distance is 2.186(2) Å, and that of Co−O ranges from 2.0740(18) to 2.0853(18) Å, showing distortion from ideal octahedra (Table

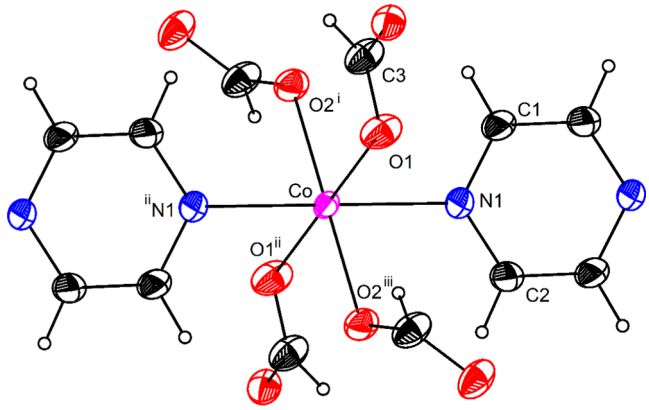

Figure 7. Crystal structure of $[Co(HCO_2)_2(pyz)]$ (**5**) showing the thermal ellipsoids drawn at the 50% probability level for all of the atoms except for the H atoms that are shown as spheres of arbitrary radii. Symmetry code: (i) $x, -y + 2, z - 1/2$ (ii) $-x + 1/2, -y + 3/2, -z + 1$ (iii) $-x + 1/2, y - 1/2, -z + 3/2$.

https://doi.org/10.1021/acsomega.1c05216
ACS Omega 2022, 7, 5698−5712

Scheme 1. Synthetic Procedure for Compounds 1−7

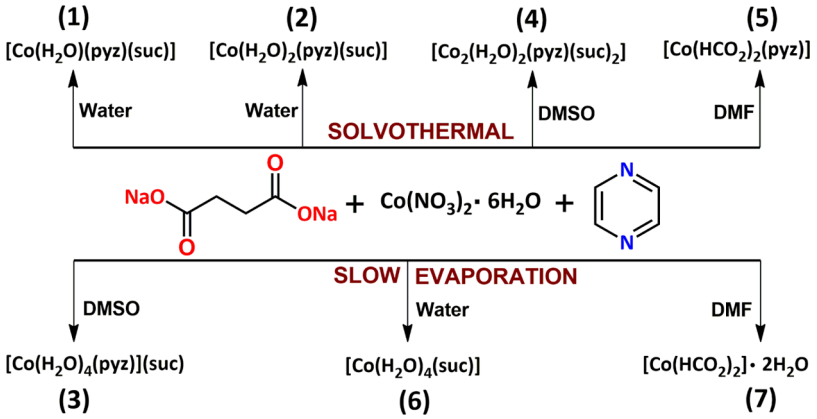

S1), which is in agreement with the reported crystal data. On viewing **5** along *c*-axis, the intrachain Co···Co distance bridged by pyz is 7.158(0) Å, while along the *a*-axis, the Co···Co distance linked via formate is 5.738(0) Å (Figure S7a,b). Formate adopts the κ-O mode to cobalt. Compound **5** shows a 3D packing of cobalt with pyz and formate along the *c*-direction (Figure S8).

The crystal structure of cobalt succinate tetrahydrate, i.e., $[Co(H_2O)_4(suc)]$ (**6**) is well documented in the literature and isostructural with Ni, Fe, Mg, and Mn analogues.[40,67−70] The refinement details for **6** are presented in Table S4. It crystallizes in the monoclinic $P21/c$ space group, where cobalt is octahedrally coordinated to two succinate oxygen atoms (O6 and O8^{i}) and four water molecules (O1w−O4w) (Figure S9). Succinate ligands adopt the anti−anti conformation with torsion angle χ[C(1)C(2)C(3)C(4)] = 173.53°, and the orientation of the carboxylate with respect to the C−C backbone of succinate generates angles [C(6)C(4)C(3)] and [C(8)C(1)C(2)] equal to 116.41 and 117.72°, respectively.[38,47] Each succinate ligates cobalt via the κ-O mode with coordination formula $AB^2M_4^1$ (Table 3). The intrachain Co···Co separation distance through the succinate bridge is 9.792(6) Å, which is in close agreement with that reported by Roy and co-workers, thereby resulting in a one-dimensional (1D) coordination network topology **2C1** with simple 2-c linear chains (Figure S10).[71] On comparing crystal structures of **1**−**7**, there is an enhancement in the dimensionality of the coordination network to 3D for structures with ratios of metal to bridging ligands of 1:2 (compounds **1** and **2**) and 1:3 (compounds **5** and **7**) in comparison to 1D coordination polymers with a ratio of 1:1 (compounds **3** and **6**). The pyz ligand usually accepts coordination mode B^2, while the succinate anion can be coordinated in different modes (B^2, T^3, K^{22}, K^4, T^{11}) or noncoordinated at all when H-bonds compete with coordination bonds. Aprotic solvents DMSO and DMF bind a part of pyz or succinic acid, tuning the content of the ligands in precipitating crystalline compounds. Li and co-workers have mentioned the role of solvents in coordination supramolecular systems. *N*,*N*-Dimethylformamide (DMF) can readily coordinate to metal centers; however, it hydrolyzes during reactions giving byproducts of formate anions and dimethylammonium cations, which can be incorporated into the structure.[72,73] In our work, we have demonstrated the in situ generation of formate from the reaction in DMF subjected to autoclave conditions, yielding **5** and **7**. We have not examined the crystal structure of **7** as under fast scan we obtained structure parameters as trigonal space group $R\bar{3}c$, with parameters $a = b = 8.1951(3)$, $c = 22.2502(17)$, $\alpha = \beta = 90°$, $\gamma = 120°$, and $V = 1294.12$ Å^3, which matched with the reported structure of **7**. Compound $(Me_2H_2N)[Co(HCOO)_3]$ (**7**) has one of the most symmetrical 3D 6-c underlying nets of topology **pcu**.[55] This net shows only three directions for spreading the edges, while edges of **rob** net spread in four directions. Such a difference in the structure of **7** is attributed to the presence of $Me_2H_2N^+$ cations in the voids.[74−77]

Syntheses and Spectroscopic Properties of 1−7. It is remarkable that the same starting materials $Co(NO_3)_2{\cdot}6H_2O$, Na_2suc, and pyz under the influence of temperature (conventional slow evaporation and hydro(solvo)thermal methods at 105 °C for 2 days) and solvent (water, DMSO, and DMF) were vital for obtaining the desired compounds (Scheme 1). Hydrothermal conditions yielded orange crystals of **1** along the walls of the Teflon vessel, and slow evaporation of the mother liquor afforded red crystals of **2**. Subjecting to steam bath heating, we obtained copious amounts of $[Co(H_2O)_4(suc)]$ (**6**) coordination polymer.[25,26] Bearing in mind the literature on aprotic solvents (DMSO and DMF) acting as linkers or guest molecules in MOFs, we simply mixed the aforesaid reagents (1:1:3) at ambient conditions in DMSO, forming bright orange crystalline blocks of **3**. Under solvothermal conditions, fine purple crystalline cubes of **4** were obtained. On allowing the filtrate to slowly evaporate at room temperature, **6** crystallized out as the secondary product. On the other hand, DMF gave an appreciable yield of **6** under normal reaction conditions. However, under solvothermal conditions, maroon blocks of **5** concomitant with purple crystals of **7** were isolated. Surprisingly, **5** contained the hydrolysis product of DMF (formate) along with pyrazine, without the incorporation of the succinate ligand as reported by Sahoo and co-workers.[39] Compound **7** obtained in larger quantity was devoid of pyrazine and succinate ligands and contained only formates coordinated to cobalt.

The infrared spectra of **1**−**4** were compared with that of **6**, as shown in Figure S11a. All of the compounds exhibited broad vibrations between ∼3230 and 3560 cm^{-1}, suggesting the presence of water molecules. Medium-to-weak absorptions between ∼2890 and 3080 cm^{-1} for all compounds are due to C−H vibrations. Strong-to-medium absorptions for **1**−**4** and **6** at ∼1500−1550 and ∼1380−1430 cm^{-1} are assigned to the asymmetric and symmetric stretching vibrations, respectively, of succinate. The separation distances between $\nu_{asym}(COO^-)$

https://doi.org/10.1021/acsomega.1c05216
ACS Omega 2022, 7, 5698−5712

and $\nu_{sym}(COO^-)$, i.e., Δ, are 144 and 161 cm^{-1} for **1** and **2**, respectively, consistent for the *bis*-bidentate coordination mode. The Δ value of 90 cm^{-1} for **4** is in accordance with the bridging coordination modes observed. For **5** and **7**, the ν_{asym} and ν_{sym} vibrations due to formate ions appear at ∼1540−1550 and ∼1330−1365 cm^{-1}, respectively (Figure S11b).[78−82]

Raman spectra of **1**−**3**, **5**, and **7** when compared with the corresponding IR spectra (Figure S12a−e) depicted in-plane bending modes of pyrazine at ∼1000 cm^{-1}. The $s(CH_2)$ scissoring band of succinate can be seen as a weak doublet at ∼1443 and ∼1415 cm^{-1}. Weak intensity at ∼1210 cm^{-1} is due to the $w(CH_2)$ wagging mode of succinate. A weak δ(OCO) bending mode of succinate is at ∼634 cm^{-1}. The symmetrical ν_{sym}(CH) vibrations at ∼2855 cm^{-1} are observed for both succinate and pyrazine along with the ν(OH) mode at ∼3560 cm^{-1}, all seen as sharp peaks.[79−81] The UV−vis absorption spectra of **1**−**6** are shown in Figure S13, and an inset displays d−d bands. The bands between ∼260 and 308 nm are assigned to $\pi-\pi^*$ and $n-\pi^*$ transitions of the linkers. The d−d band at ∼510 nm corresponds to $^4T_{1g}(F) \rightarrow {}^4T_{1g}(P)$ transition for a distorted octahedral Co(II) center.[82,83]

*Magnetic Properties of **1**−**5**.* We resorted to studying the magnetic properties in the solid state by performing temperature-dependent magnetic susceptibility (χ_M) measurements on the finely powdered samples of **1**−**5** under an applied magnetic field of 100 Oe in the temperature range of 60−310 K. The plot of χ_M versus T shows the influence of temperature on the zero-field-cooled−field-cooled (ZFC−FC) curves. In the case of **1** (Figure 8), the magnetic susceptibility (χ_M)

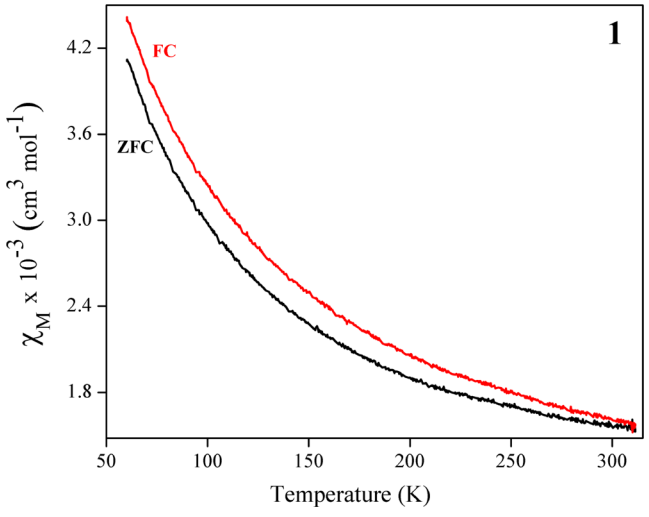

Figure 8. Plot of zero-field-cooled (ZFC)−field-cooled (FC) magnetic susceptibility for **1** as a function of temperature under an applied field of 100 G between 60 and 310 K.

values were found to increase monotonically with decreasing temperature (i.e., high χ_M values at 60 K). The ZFC−FC curves displayed an appreciable extent of bifurcation suggestive of magnetic ordering. This trend is also pronounced in all of the compounds (Figure S14a for **4**). Hence, the higher χ_M values for FC measurements are due to the unpaired electron spins aligned with respect to the applied magnetic field (100 Oe), while lower χ_M values in the ZFC situation are attributed to randomization of spins due to the absence of applied field.[46,72]

Moreover, the curve of $\chi_M T$ against T for **1**−**5** presented a continuous decrease of $\chi_M T$ values upon cooling. As seen in the case of **4** (Figure S14b), the $\chi_M T$ value descended from 1.180 cm^3 mol^{-1} K at 310 K to 0.605 cm^3 mol^{-1} K on cooling to 60 K. This outcome is relevant to cobalt(II) compounds, suggesting magnetic exchange interactions between the cobalt(II) centers. From the crystal structure analysis (vide infra), the cobalt(II) centers are bridged by suc^{2-} as well as pyz along different dimensions for **1**, **2**, and **4**, while only pyz bridges the cobalt(II) centers in **3**, along with bridging pyz and formate in **5**. The average Co···Co distance flanked by pyrazine is 7.2 Å, which is sufficiently good for magnetic interactions to take place. These observations draw conclusions from single-ion anisotropy and antiferromagnetic (AF) interactions mediated by ligands bridging the cobalt(II) centers.[42,43,48,61] So, to gather evidence on the AF interactions persisting in the compound, we performed various temperature susceptibility (χ_M) measurements on compound **1**. From the plot of χ_M versus T (Figure S15a), there was a gradual decrease in χ_M from 0.136 cm^3 mol^{-1} at RT to 0.00854 cm^3 mol^{-1} at 298 K with effective magnetic moment calculated using $\mu_{eff} = 2.82(\chi_M T)^{1/2}$ of 4.5 BM, which deviates from the calculated spin-only magnetic moment (μ_{so} = 3.87 BM) for a high-spin Co(II) $3d^7$ system with $S = 3/2$. The plot of χ_M^{-1} versus T (Figure S15b) was essentially linear over the entire temperature range following the Curie−Weiss law given as follows: $\chi_M = \frac{C}{T-\phi}$, where χ_M is the magnetic susceptibility in cm^3 mol^{-1}, C is the Curie constant, T is the temperature in kelvin, and ϕ is the Weiss constant in kelvin. A fitting of the Curie−Weiss law on the data gave a Curie constant (C) of 2.525 obtained from the inverse of the slope and a negative Weiss constant (ϕ) of −46.24 K, suggesting weak antiferromagnetic (AF) exchange interactions. The declining $\chi_M T$ values upon cooling confirm this behavior. The effective magnetic moment calculated using $\mu_{eff} = (8C)^{1/2}$ was 4.51 BM.[38,72]

Thermogravimetric Analyses, X-ray Powder Diffraction Patterns, and Gas Adsorption Properties. We investigated the thermal stability of **1**−**7** by TG−DTG measurements in the temperature range of 30−650 °C. The TG curve of **1** shows a mass loss of 6.1% from 32 to 85 °C due to water (calcd 6.6%). On increasing the temperature up to 345 °C, there was gradual degradation of pyrazine and succinate to 68.5% (calcd 71.8%) as evidenced by peaks at 200 and 345 °C in DTG; a residue of 23.6% (calcd 27.4%) was obtained for CoO (Figure 9).

Compound **2** is stable up to 110 °C and thereafter disintegrates to give a mass loss of 12.5% due to two water molecules (calcd 12.36%), evident at 150 °C in DTG. Pyrazine decomposes to 26.46% (calcd 27.48%) followed by succinate to 39.84% (calcd 35.83%), indicated at 332 °C in DTG. A residue of 26.17% corresponding to CoO (calcd 25.76%) is obtained (Figure S16a). Compound **3** is stable until 90 °C followed by a mass loss of 22.5% at 135 °C due to the elimination of four water molecules (calcd 22.0%). This is associated with the corresponding peak at 132 °C in DTG. The dehydrated compound then disintegrates to a total mass loss of 57.1% due to ligand decomposition (calcd 59.9%), evident at 342 °C in DTG, giving a residue of 20.1% of CoO (Figure S16b). In the case of **4**, stability up to 80 °C with two subsequent weight losses of 25.73% from 90 to 200 °C and 51.6% up to 400 °C can be assigned to the concomitant loss of two water molecules, pyrazine (calcd 24.88%) and succinate (calcd 49.77%) as confirmed by DTG peaks at 202 and 366

https://doi.org/10.1021/acsomega.1c05216
ACS Omega 2022, 7, 5698−5712

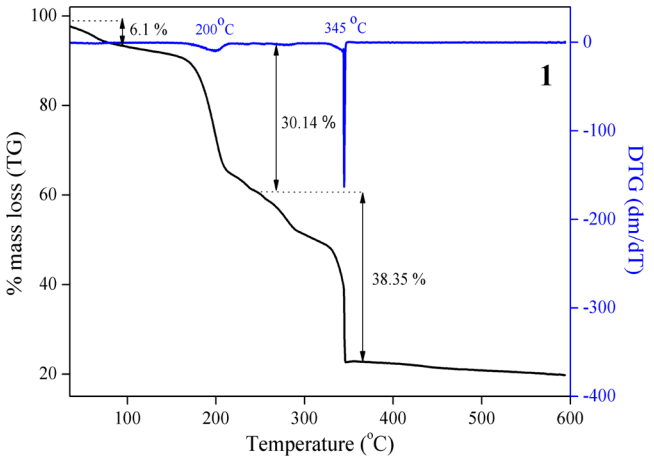

Figure 9. TG−DTG plot of **1** recorded between 30 and 600 °C in air at 10 °C min^{-1}.

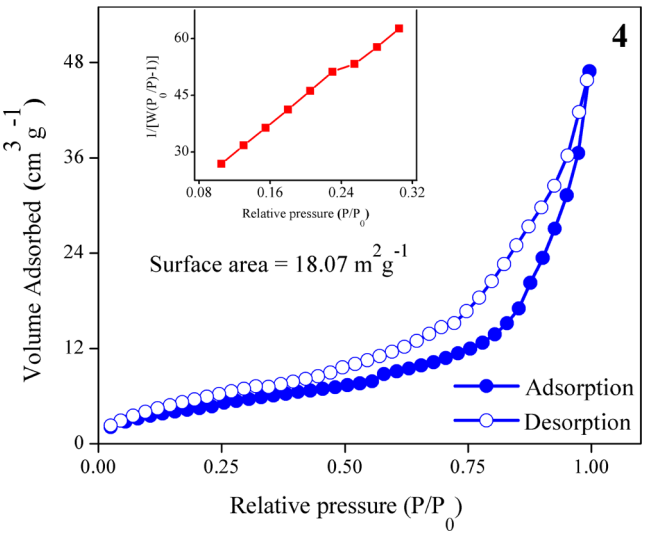

Figure 10. Nitrogen adsorption/desorption isotherms at 77 K for **4** displaying the highest surface area; filled spheres, adsorption; empty spheres, desorption (inset: BET plot).

°C, respectively. A residue of 17.65% of CoO was formed (Figure S16c). Compound **5** recorded the highest stability of 250 °C and thereafter decomposes until 315 °C to 66.0% (calcd 74.30%) due to the loss of formate (CO_2, water, and CO) and pyrazine as characterized by a sharp DTG peak at 306 °C, with a residue of 33.48% (Figure S16d). Cobalt(II) succinate tetrahydrate **6** shows thermal stability up to 80 °C followed by a sharp weight loss of 30.23% between 78 and 130 °C due to four water molecules (calcd 29.14%). This is associated with a corresponding peak at 130 °C in DTG. The dehydrated compound is stable up to 320 °C and then abruptly disintegrates until 340 °C with a mass loss of 40.1% (calcd 40.5%), assignable to ligand decomposition with a sharp peak at 345 °C in DTG. The final decomposed product of 28.6% is probably CoO (Figure S16e). The thermal pattern of **7** is associated with the loss of two water molecules at 19.3% (calcd 19.47%) followed by subsequent decomposition of formate up to 300 °C of 46.13% (calcd 48.67%) with a residue of 35.32% of CoO (Figure S16f).

Thermal analyses of **1**−**7** revealed moderate to high thermal stabilities, and, crystal structural analyses revealed diverse architectures with the presence of minute pores as visualized by the crystal structure visualization tool (Mercury 4.2).[84] This observation lies on the fact that MOFs possess the properties of modest thermal stability and robust architecture, thereby serving as traps for selective gas adsorption. Here, we investigated the CO_2 and N_2 adsorption properties of our compounds to determine their porosity. In adsorption studies, the compounds were degassed at 80 °C for ∼15 h to ensure that the samples were free from adsorbed moisture. The N_2 and CO_2 adsorption performance was then investigated for the degassed samples **1**−**7** at 77 and 298 K, respectively. The reversible N_2 sorption profiles for **4** at 77 K (Figure 10) demonstrate type III adsorption isotherm behavior (characteristic of non/macroporous substances) with a modest uptake value of ∼47 $cm^3\ g^{-1}$, suggesting only surface adsorption. The BET surface area (Figure 10, inset) and total pore volume of **4** are 18.07 $m^2\ g^{-1}$ and 0.072 $cm^3\ g^{-1}$, respectively. The reversible N_2 sorption plots for the other compounds are shown in Figure S17. The adsorption and desorption curves do not agree with each other, indicating a type H3 hysteresis loop (according to the IUPAC classification). The N_2 uptake values have been found as 5.54 (**1**), 12.54 (**2**), 29.32 (**3**), 47.40 (**4**), 34.60 (**5**), and 22.11 (**6**) $cm^3\ g^{-1}$ at P/P_0 ∼0.99. All of the compounds show a negligible amount of N_2 uptake with a type III surface adsorption isotherm, thereby having low BET surface areas of 3.53, 9.12, 10.52, 18.07, 9.28, 11.16, and 2.75 $m^2\ g^{-1}$ for **1**−**7**, respectively (Table S5). The observed pore volumes in $cm^3\ g^{-1}$ are 0.008 (**1**), 0.019 (**2**), 0.072 (**4**), and 0.034 (**6**). However, the formate containing compounds **5** and **7** had pore volumes of 0.053 and 0.010 $cm^3\ g^{-1}$, respectively. The calculated pore volumes for **1**−**6** are 64.76, 40.66, 48.08, 14.66, 51.80, and 9.85 in $Å^3$, respectively, as obtained from Mercury 4.2. The low N_2 uptake could stem from the fact that the low thermal energy of N_2 at 77 K makes it unable to overcome the high diffusion barrier, thereby causing N_2 gas to escape.

A similar phenomenon was observed for CO_2 gas adsorption, resulting in very low uptake due to the blocking of the windows of unidirectional pores to the incoming CO_2 molecules. The CO_2 adsorption isotherms recorded at 298 K showed adsorption of 15.22 $cm^3\ g^{-1}$ for **1**, 4.09 $cm^3\ g^{-1}$ for **2**, 5.80 $cm^3\ g^{-1}$ for **3**, and 4.46 $cm^3\ g^{-1}$ for **4**, while the formate counterparts, **5** and **7** exhibited CO_2 uptake of 4.18 and 3.32 $cm^3\ g^{-1}$, respectively. Cobalt succinate tetrahydrate **6** exhibited a CO_2 uptake of 6.57 $cm^3\ g^{-1}$ (Figure 11). The desorption curves did not trace the adsorption curves and showed hysteretic nature due to the strong interaction of CO_2 molecules with the framework on account of the strong quadrupole moment of CO_2. The adsorption profiles were of type III with poor sorption, suggesting strong attraction of gaseous adsorbate to the pore surface, thereby preventing interaction of other molecules.[85−88]

The X-ray powder diffraction patterns of the bulk samples of compounds **1**−**6** were measured and compared with the calculated X-ray powder patterns obtained from Mercury 4.2. Both experimental and calculated X-ray powder patterns of compounds **3**, **4**, and **6** perfectly matched, while those of others (**1**, **2** and **5**) showed trace impurities, which are evident from profile fitting of the powder patterns using the Le Bail method with the help of FullProf software (Figures S18−S23).[89,90] After understanding the X-ray powder patterns of **1**−**6**, they were further inspected for surface morphology using scanning electron microscopy (SEM). The SEM images were

https://doi.org/10.1021/acsomega.1c05216
ACS Omega 2022, 7, 5698−5712

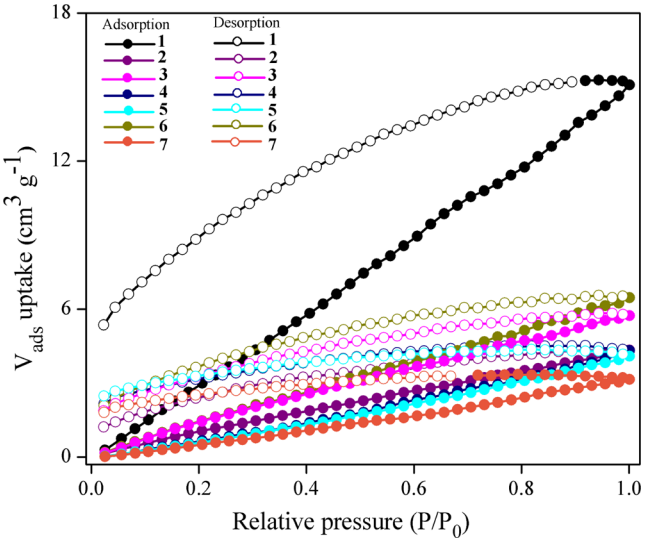

Figure 11. Carbon dioxide sorption isotherms at 298 K for **1**−**7** (filled spheres, adsorption; empty spheres, desorption).

obtained at 20 kV with a magnification of up to 40 000× (Figure S24). The morphological examination of the powdered sample of **1** showed well-defined octahedral-shaped particles, while the SEM image of **2** showed particles arranged as small rods with irregular edges. Compound **3** exhibited globular-shaped particles with agglomeration; on the other hand, well-defined rectangular plates stacked onto each other to form bundles were observed for compound **4**. Only formate- and pyrazine-containing compound **5** appeared as agglomerated rod-shaped particles along with irregular globular-shaped particles; similarly, succinate- and hydrate-containing **6** also showed particles of irregular shape and varying size. Formate compound **7** exhibited a morphology in which the particles were viewed as well-defined rectangular rods along with lozenge-shaped particles (Figure S24).[85−88] With complete characterization on structural and morphological aspects, we then diverted our attention to understanding the luminescence properties of compound **1** as the results obtained for **2** and **3** did not show any pronounced difference. It was observed that succinic acid showed an emission band at 393 nm due to the $\pi^* \rightarrow$ n or $\pi \rightarrow \pi^*$ transitions upon excitation at 350 nm.

Fluorescence Sensing Properties of 1. The fluorescence properties of **1** in the solid state and as a suspension in water and DMSO were investigated. As a suspension in water and DMSO, **1** emitted strongly at 345 nm upon excitation at 300 nm, while the solid-state spectra for **1** showed emission at 428 nm upon excitation at a longer wavelength of 370 nm (Figure S25a,b). These emissions are likely attributed to the $\pi^* \rightarrow$ n or $\pi \rightarrow \pi^*$ transitions arising from the succinate ligand.[50] Hence, we observed a blue shift (decrease in λ) on moving from solid-state fluorescence emission to the suspension phase.

For the fluorescence sensing titrations, 2 mL of aqueous suspension of **1** (2 mM) was placed in a quartz cell of 1 cm width and aqueous solution of NAC (1 mM) was added gradually in an incremental fashion of 10 μL. The emission spectra were recorded upon excitation at 300 nm at 298 K, and the corresponding emission wavelength at 345 nm was monitored. Both the excitation and emission slit widths were 10 nm for all of the measurements. Each titration was repeated at least three times to obtain concordant values. From the fluorescence sensing experiments, we observed consistent emission spectra for **1** in water (ex. 300 nm, em. 345 nm) upon addition of NACs with gradual decay of the emission band; unlike for DMSO showing a drastic shift in λ upon the same excitation with NAC addition (Figure S26). Hence, water was chosen as the medium for carrying out sensing experiments. The relative fluorescence emission spectra were measured for an aqueous suspension of **1** in various analytes (NACs) used as a quencher in water. In the current study, the NACs employed were nitrobenzene (NB), *o*-nitrotoluene (*o*-NT), *p*-nitrotoluene (*p*-NT), *o*-nitrophenol (*o*-NP), *p*-nitrophenol (*p*-NP), 2,4-dinitrophenol (DNP), and 2,4,6- trinitrophenol (TNP). No change was observed in the shape of the emission spectra of **1**, although only quenching of the initial fluorescence emission intensity upon titration with the electron-deficient NACs was seen. The representative titration of *p*-NP with **1** is shown in Figure 12, while titration with other NACs is provided in the Supporting Information (Figures S27 and S28).

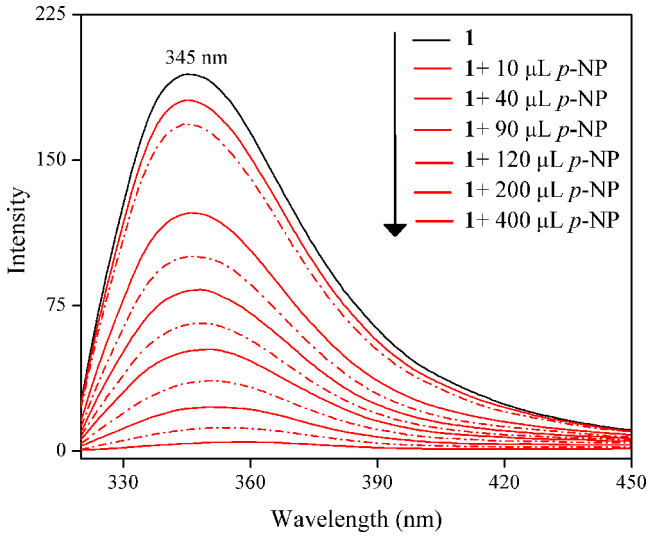

Figure 12. Reduction of the fluorescence emission of **1** upon gradual addition of 1 mM *p*-nitrophenol (*p*-NP).

In all cases, the initial fluorescence intensity of **1** was found to show a considerable decrease upon gradual addition of the NACs. The fluorescence efficiency (η) was calculated as $[(I_0 - I)/I_0] \times 100\%$, where I_0 and I are the fluorescence intensities before and after addition of the respective NACs. The initial emission intensity of **1** was quenched by approximately 98% (η) after the addition of 400 μL of *p*-NP. On the other hand, a sluggish decline in the intensity of **1** was observed with only 26% quenching with the addition of 410 μL of NB. The addition of 500 μL of *o*-NT gave 7.4% quenching. The emission intensity decreased to a minimum at 69% quenching efficiency with the addition of 740 μL of *p*-NT. Furthermore, the intensity of **1** was quenched to 82% after adding 950 μL of *o*-NP. On adding DNP (300 μL), there was 86% quenching of the emission intensity of **1**. Moreover, the addition of TNP (380 μL) showed 94% quenching of the emission intensity of **1**. Therefore, in terms of fluorescence quenching efficiencies, the NACs follow the trend *o*-NT < NB < *p*-NT < *o*-NP < DNP < TNP < *p*-NP. Hence, **1** was found to show remarkably higher efficiencies toward nitrophenols with 98% for *p*-NP than the nitrotoluene compounds. The sensing ability of **1** toward the different NACs is plotted in terms of their quenching

https://doi.org/10.1021/acsomega.1c05216
ACS Omega 2022, 7, 5698−5712

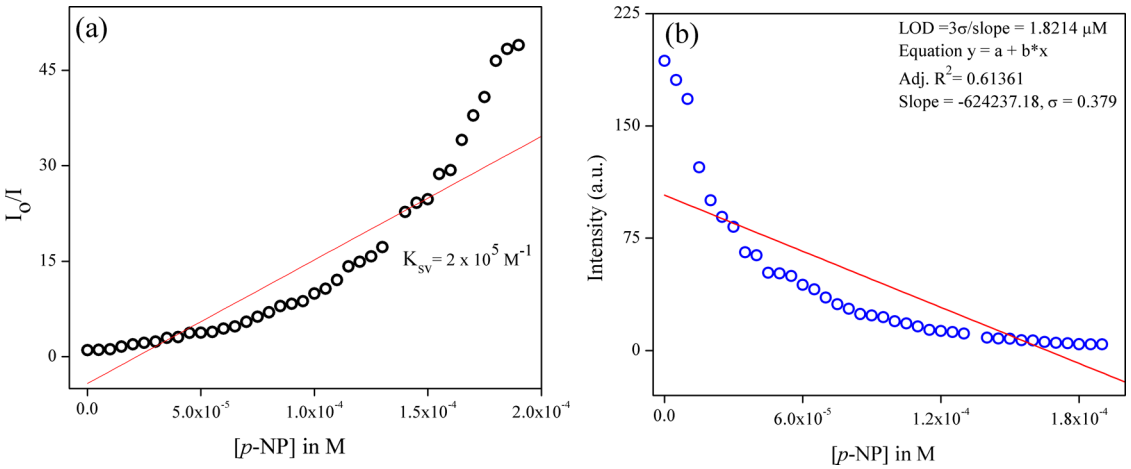

Figure 13. (a) Stern−Volmer plot for **1** with *p*-NP exhibiting the highest K_{sv} value among other NACs. (b) Plot for the determination of the limit of detection (LOD) for *p*-NP.

efficiencies (%), as depicted in Figure S29. Thus, it unambiguously suggests that **1** can be selectively used as a chemical sensing reagent in the detection of *p*-NP from an aqueous mixture of other NACs.[91−95]

The Stern−Volmer quenching constant (K_{sv}) was calculated employing the normalized fluorescence emission intensity (I_0/I) as a function of increasing quencher concentration [Q] by the following relation; $I_0/I = 1 + K_{sv}$ [Q], where I_0 and I are the emission intensities of **1**, before and after addition of NACs, respectively, K_{sv} is the quenching constant (M^{-1}), and [Q] is the molar concentration of NACs. The Stern−Volmer plot of **1** with *p*-NP is depicted in Figure 13a, while that with the other NACs are provided in the Supporting Information (Figure S30). It can be seen that that Stern−Volmer plot followed a linear path at low concentrations; however, at higher concentrations, the linearity deviated as an upwardly bent curve as a consequence of static and collisional quenching mechanisms. The K_{sv} values for **1** toward all of the NACs used are given in Table 4. The quenching constant for *p*-NP was

Table 4. Quenching Efficiencies, Stern−Volmer Constants, and LODs upon Addition of Different NACs to 1

				limit of detection (LOD)	
sr. no.	NAC	quenching efficiency η (%)	Stern−Volmer constant K_{sv} (M^{-1})	μM	ppm
1	NB	26	1.1×10^3	14.026	7.661
2	*o*-NT	7.4	3.3×10^2	32.480	17.741
3	*p*-NT	69	5×10^3	5.000	2.731
4	*o*-NP	82	7×10^3	7.680	4.195
5	*p*-NP	98	2×10^5	1.821	0.995
6	DNP	86	2.8×10^4	3.053	1.668
7	TNP	94	5.7×10^4	3.242	1.771

200 times greater than that for the simplest NB, while *p*-NP showed K_{sv} values about 29, 6.5, and 3.5 times greater than the nitrophenol compounds (*o*-NP, DNP, and TNP), respectively. This signified the exclusive quenching ability of *p*-NP toward luminescent **1** in water among other NACs.[95−98]

Determining the Limit of Detection (LOD). The LOD was calculated from the plot of fluorescence intensity with increasing concentration of NACs. The slope of the line (m) was calculated from the plot, while the standard deviation (σ) was taken from three blank measurements of **1**. The LOD was calculated based on the following formula: $3\sigma/m$. The LOD could be expressed in molar or ppm (parts per million), as calculated in Figure S31 and Table 4. The limit of detection of *p*-NP was found to be as low as 0.995 ppm or 1.821 μM (Figure 13b). This clearly depicts that **1** has high selectivity for *p*-NP over the other potentially interfering NACs.[95,98]

With a view to understanding the mechanism prevailing between **1** and respective NACs, we recorded the absorption spectra of the individual NACs and the completely quenched mixture (**1** + NAC); the observations are summarized in Table S6 and Figure S32, displaying red and blue shifts with no new peak formation. Thus, we speculated dynamic quenching since the fluorophore (**1**) was quenched on collision with the quencher (NAC) without formation of a new species. However, from the S−V plot showing deviation in linearity, we could infer that both static and collisional quenching mechanisms are active. We can rule out the encapsulation of NACs in the pores of **1** as evident from the low surface properties of **1** already discussed in the previous section (vide supra). Due to the dispersible nature of the microsized fine particles of **1** in water, there was close contact with NACs, thus relating the fluorescence turn-off (quenching) to the photo-induced electron transfer (PET) mechanism. Generally in PET, the conduction band (CB) of **1** lies at higher energy than the LUMOs of the NACs to facilitate electron transfer, thereby favoring effective quenching. Apart from this, the nonlinear nature of S−V plots for the NACs also suggested the resonance energy transfer (RET) mechanism for enhanced quenching. The probability of RET depended on the extent of spectral overlap between the absorption band of the NACs and the emission band of **1**. As can be seen in Figure 14, the absorption spectra of *p*-NP, TNP, and DNP showed a considerable overlap with the 345 nm emission band of **1**, while marginal or no spectral overlap is observed for the other NACs. As a result, high quenching responses were observed for *p*-NP (98%), TNP (94%), and DNP (86%) compared to the rest of the NACs. These furnished the fact that the concomitant effect of PET and RET mechanisms is responsible for the effective fluorescence quenching of **1** by the NACs. Thus, **1** responded more selectively to *p*-NP than the other NACs with a quenching efficiency of 98%.[31,94,96−100]

https://doi.org/10.1021/acsomega.1c05216
ACS Omega 2022, 7, 5698−5712

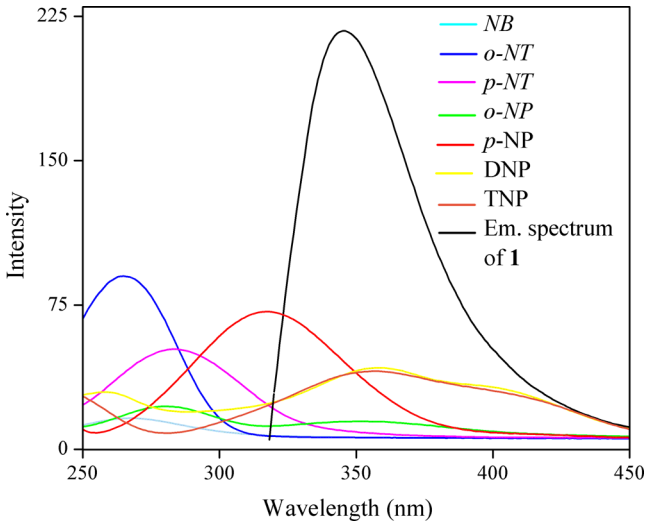

Figure 14. Spectral overlap between the absorption spectra of NACs and the emission spectrum of **1** in water.

CONCLUSIONS

We explored the chemistry of cobalt(II) with pyrazine (rigid) and succinic acid (flexible) in water/DMSO/DMF under ambient/solvothermal conditions generating CPs with diverse architectures (1D to 3D). The construction of CPs was influenced by different binding modes adopted by the carboxylate ligand and the μ_2 bridging mode of pyrazine, mediated by the reaction conditions. The topologies of the coordination polymers **1**−**7** were described by underlying nets 3D 3,5-c **fet**, 3D 4-c **cds**, 1D 2-c **2C1**, 3D 5-c **bnn**, 3D 6-c **rob**, 1D 2-c **2C1**, and 3D 6-c **pcu**, respectively. The plot of χ_M^{-1} versus T was essentially linear over the entire temperature range following the Curie−Weiss law with a Curie constant (C) = 2.525 and a negative Weiss constant (ϕ) = −46.24 K, suggesting weak antiferromagnetic (AF) exchange interactions. The gas adsorption measurements revealed a type III isotherm, indicating the macroporous nature of the compounds. Scanning electron microscopy images presented assorted surface morphologies. The present data unambiguously suggested that **1** can be selectively used as a chemical sensing reagent in the detection of p-NP (highest η) from a mixture of NACs, with a detection limit of 0.995 ppm for *p*-NP. The Stern−Volmer plot exhibited deviation in linearity with K_{sv} values about 200 times greater than that for the simplest nitroaromatic compound (NB), signifying its exclusive quenching ability toward **1**.

EXPERIMENTAL SECTION

Materials and Instrumentation. All chemicals and solvents were commercially available and used as received. The disodium salt of succinic acid (Na_2suc) was prepared by the slow addition of $NaHCO_3$ to the hot aqueous solution of succinic acid (2:1), followed by slow evaporation to give white crystalline flakes. The composition of Na_2suc was studied by IR spectroscopy and elemental analysis (C, H, and N). Necessary safety measures were taken during autoclave syntheses using Teflon-lined stainless steel vessels heated in a temperature-controlled oven (ANTS make). The IR spectra of powdered compounds **1**−**7** were recorded on dilution with KBr on a Shimadzu (IR Prestige-21) FTIR spectrometer in the region 4000−350 cm^{-1} at 4 cm^{-1} resolution. Solid-state Raman spectra were measured using 785 nm laser radiation for excitation with the laser power set to 100 mW on an Agiltron PeakSeeker Pro Raman instrument using a 1 mm quartz cell. The absorption spectra were recorded on an Agilent UV−vis spectrophotometer (Model 8453). Elemental analyses (C, H, and N) were performed on an Elementar Variomicro Cube CHNS analyzer. The field-dependent magnetization studies, viz., zero-field cooling (ZFC) and field cooling (FC), were performed between temperatures 60 and 310 K under an applied magnetic field of 100 G. The variable-temperature magnetic susceptibility data for only **1** was obtained on a vibrating sample magnetometer (VSM) with the sensitivity of a SQUID (Superconducting Quantum Interference Device) magnetometer. The SQUID-VSM magnetometer (Quantum Design, MPMS-3) was operated in the temperature range of 10−300 K under an applied field of 1000 G. Thermogravimetric analysis (TG−DTG) were carried out on a PerkinElmer TGA 4000 analyzer in air at a heating rate of 10 °C min^{-1} from room temperature to 650 °C. Powder X-ray diffraction (PXRD) data were collected on a Bruker D8 Advance X-ray diffractometer using Cu Kα_1 (λ = 1.5406 Å) with a Ni filter. Surface morphologies of the compounds were evaluated on a Carl-Zeiss Evo scanning electron microscope (SEM) operating at 20 kV. The solution-state fluorescence spectra were recorded on a Cary Eclipse fluorescence spectrophotometer. The ambient pressure volumetric N_2 adsorption−desorption measurements were performed at 77 K maintained by low-temperature liquid nitrogen Dewar and those of CO_2 were performed at 298 K in the pressure range 0−760 Torr using an AutosorbiQ (Quantachrome Inc.) gas sorption analyzer. Before analysis, **1**−**7** were soaked in chloroform for 24 h to remove water molecules. Subsequently, the supernatant chloroform was poured and the procedure was repeated twice with fresh chloroform. Further, the outgassing process was carried out at 80 °C for 15 h under a dynamic vacuum of 10^{-3} Torr until a stable weight was obtained. Warm and cold free space correction measurements were carried out utilizing ultrapure (99.999% purity) He gas. For analysis, high-purity (99.999%) N_2 and CO_2 were used, which were again purified by calcium aluminosilicate adsorbents to remove any trace amounts of moisture before analysis. The adsorption data in the pressure range <0.1 P/P_0 were fitted to the Brunauer−Emmett−Teller (BET) equation to determine the surface area. The fluorescence spectra of **1** in the solid state and in suspension in water and DMSO were recorded by a xenon flash lamp technology-based Cary Eclipse Fluorescence Spectrophotometer (G9800A) from Agilent Technologies. For nitroaromatic compound (NAC) sensing, 2 mM suspension of **1** in 2 mL of DMSO/water was placed in a 1 cm quartz cuvette, to which an aqueous solution of 1 mM NAC was added. Excitation was carried out at 300 nm with slit widths of excitation and emission of 10 nm, respectively.

Synthesis of [Co(H_2O)(pyz)(suc)] (1) and [Co(H_2O)$_2$(pyz)-(suc)] (2). An aqueous solution (2 mL) of $Co(NO_3)_2{\cdot}6H_2O$ (1 mmol, 0.291 g) was added dropwise to an aqueous mixture (3 mL) of disodium succinate (1 mmol, 0.162 g) and pyrazine (3 mmol, 0.24 g). The orange solution was stirred at room temperature (RT) for 30 min and then transferred into a 10 mL Teflon-lined stainless steel autoclave, which was heated to 105 °C for 48 h. On cooling, orange plate-shaped crystals of **1** deposited along the walls of the Teflon cup separated from the mother liquor and were air-dried (yield = 0.085 g). Slow evaporation of the mother liquor at room temperature gave red

https://doi.org/10.1021/acsomega.1c05216
ACS Omega 2022, 7, 5698−5712

crystalline blocks of **2**, which were isolated and air-dried (yield: 0.23 g).

Anal. Calcd for **1** $C_8H_{10}N_2O_5Co$ (Mr. = 273.11): C, 35.18; H, 3.69; N, 10.26. Found: C, 35.02; H, 3.67; N, 10.12. IR (KBr, cm^{-1}): 3223 (br), 2890 (m), 2323 (m), 1656 (w), 1542 (s), 1430 (m), 1328 (w), 1243 (m), 1170 (m), 1045 (m), 1040 (w), 975 (m), 890 (w), 801 (w), 678 (m), 540 (m), 420 (w). UV−vis in water (λ_{max} nm, ϵ): 267 (6520), 308 (860), 510 (7), 641 (1).

Anal. Calcd for **2** $C_8H_{12}N_2O_6Co$ (Mr. = 291.13): C, 33.01; H, 4.15; N, 9.62. Found: C, 33.52; H, 4.07; N, 9.63. IR (KBr, cm^{-1}): 3340 (br), 2907 (m), 2423 (m), 1520 (s), 1360 (s), 1260 (m), 1190 (m), 1130 (m), 1030 (m), 763 (m), 610 (m), 520 (m), 412 (m). UV−vis in water (λ_{max} nm, ϵ): 263 (14872), 306 (1624), 470 (13), 510 (15).

*Synthesis of [Co(H$_2$O)$_4$(pyz)$_2$](suc) (**3**).* Compound **3** was synthesized using the same reactants as those for **1** and **2**, except that DMSO/H_2O (5 mL, v/v, 3:2) was used instead of H_2O and the reaction was performed at room temperature with stirring for 30 min. Elongated bright orange crystalline blocks of **3** started to grow after 2 days, which were isolated and air-dried (yield: 0.37 g).

Anal. Calcd for **3** $C_8H_{16}N_2O_8Co$ (Mr. = 327.16): C, 29.37; H, 4.93; N, 8.56. Found: C, 29.12; H, 5.10; N, 8.12. IR (KBr, cm^{-1}): 3250 (br), 2990 (m), 2230 (m), 1895 (m), 1840 (m), 1873 (s), 1710 (w), 1630 (m), 1490 (s), 1380 (s), 1260 (m), 1130 (m), 1060 (m), 1100 (m), 940 (w), 835 (w), 790 (w), 760 (w), 640 (m), 570 (m), 430 (m). UV−vis in water (λ_{max} nm, ϵ): 265 (7480), 308 (860), 478 (6), 510 (7).

*Synthesis of [Co$_2$(H$_2$O)$_2$(pyz)(suc)$_2$] (**4**).* The synthesis method was similar to those of **1** and **2** under autoclavable conditions, except that DMSO/H_2O (5 mL, v/v, 3:2) was used instead of H_2O. Purple crystals of **4** were obtained after 2 days along with pink crystalline blocks of compound **6**. The crystals of **4** were first picked by a stainless steel spatula and then air-dried (yield = 0.192 g). The remaining pink crystals of **6** were isolated by filtration and air-dried (yield = 0.324 g).

Anal. Calcd for **4** $C_{12}H_{16}N_2O_{10}Co_2$ (Mr. = 466.13): C, 30.92; H, 3.46; N, 6.01. Found: C, 30.45; H, 3.27; N, 5.97. IR (KBr, cm^{-1}): 3380 (br), 2895 (m), 2290 (m), 1970 (m), 1890 (m), 1680 (m), 1540 (s), 1441 (s), 1306 (m), 1180 (m), 1100 (m), 1070 (m), 995 (m), 850 (w), 670 (m), 471 (m). UV−vis in water (λ_{max} nm, ϵ): 264 (463), 304 (52), 474 (15), 512 (5).

Anal. Calcd for **6** $C_4H_{12}O_8Co$ (Mr. = 247.07): C, 19.45; H, 4.90. Found: C, 19.40; H, 4.91. IR (KBr, cm^{-1}): 3330 (br), 2889 (m), 2440 (m), 1660 (m), 1650 (w), 1555 (s), 1473 (w), 1411 (s), 1350 (m), 1290 (m), 1250 (m), 1190 (m), 1050 (m), 980 (w), 888 (w), 672 (w), 530 (w), 415 (m). UV−vis in water (λ_{max} nm, ϵ): 202 (19050), 267 (678), 516 (31).

*Synthesis of [Co(HCO$_2$)$_2$pyz] (**5**).* The synthesis method was similar to those of **1** and **2** under autoclavable conditions, except that DMF/H_2O (5 mL, v/v, 3:2) was used instead of H_2O. After 2 days, a mixture of two compounds containing dark red and purple crystals was formed in the solution. The red crystalline blocks of **5** were isolated first using a spatula and air-dried (yield = 0.181 g). Purple crystals of **7** were then filtered and dried in air (yield = 0.252 g).

Anal. Calcd for **5** $C_6H_6N_2O_4Co$ (Mr. = 229.06): C, 31.46; H, 2.64; N, 12.23. Found: C, 30.23; H, 2.17; N, 12.1. IR (KBr, cm^{-1}): 3050 (m), 2998 (w), 2896 (m), 2800 (s), 2680 (m), 2400 (w), 2260 (w), 1910 (m), 1840 (m), 1730 (w), 1530 (s), 1370 (m), 1320 (s), 1100 (m), 1070 (m), 997 (m), 940 (m), 740 (m), 422 (m). UV−vis in water (λ_{max} nm, ϵ): 267 (868), 307 (193), 650 (6).

Anal. Calcd for **7** $C_2H_6O_6Co$ (Mr. = 126.02): C, 19.06; H, 4.76. Found: C, 18.95; H, 4.43. IR (KBr, cm^{-1}): 3320 (br), 2930 (m), 2880 (m), 2400 (m), 1910 (w), 1530 (s), 1360 (s), 1260 (m), 1190 (m), 1133 (m), 1010 (w), 740 (m), 850 (m), 760 (m), 610 (m), 520 (m), 450 (m).

■ ASSOCIATED CONTENT

Supporting Information

The Supporting Information is available free of charge at https://pubs.acs.org/doi/10.1021/acsomega.1c05216.

FTIR, Raman, and UV−vis spectra; bond measurements and angles for **1**−**6**; hydrogen bond measurements for **1**−**6**; comparative table of bond measures and synthesis method of synthesized compounds **1**−**6** with that of literature reported compounds; crystal structures of compounds **1**−**6**; crystal refinement details of **5** and **6**; thermogravimetric analysis, magnetic properties, adsorption data, PXRD patterns, and Le Bail fitting; SEM images; and fluorescence spectral data for **1** (PDF)

Crystallographic data for [Co(H$_2$O)(pyz)(suc)] (CIF)

Crystallographic data for [Co(H$_2$O)$_2$(pyz)(suc)] (CIF)

Crystallographic data for [Co(H$_2$O)$_4$(pyz)](suc) (CIF)

Crystallographic data for [Co$_2$(H$_2$O)$_2$(pyz)(suc)$_2$] (CIF)

Crystallographic data for [Co(HCOO)$_2$(pyz)] (CIF)

Crystallographic data for [Co(H$_2$O)$_4$(suc)] (CIF)

Accession Codes

CCDC Numbers 2098543, 2098544, 2098545, 2098548, 2098547, and 2098546 contain the supplementary crystallographic data of compounds **1**−**6** reported in this work, and this data can be obtained free of charge via www.ccdc.cam.ac.uk/data_request/cif or by emailing data_request@ccdc.cam.ac.uk or by contacting The Cambridge Crystallographic Data Centre, 12 Union Road, Cambridge CB2 1EZ, U.K.; fax: +44 1223 336033.

■ AUTHOR INFORMATION

Corresponding Author

Sunder N. Dhuri − *School of Chemical Sciences, Goa University, Goa 403 206, India;* orcid.org/0000-0003-2732-880X; Email: sndhuri@unigoa.ac.in

Authors

Luann R. D'souza − *School of Chemical Sciences, Goa University, Goa 403 206, India*

Nikita N. Harmalkar − *School of Chemical Sciences, Goa University, Goa 403 206, India*

Sarvesh S. Harmalkar − *School of Chemical Sciences, Goa University, Goa 403 206, India*

Sakharam B. Tayade − *Department of Chemistry, Savitribai Phule Pune University, Pune 411 007, India*

Complete contact information is available at: https://pubs.acs.org/10.1021/acsomega.1c05216

Notes

The authors declare no competing financial interest.

■ ACKNOWLEDGMENTS

S.N.D. gratefully acknowledges the financial support from CSIR (Grant No. 01(2923)/18/EMR-II). The authors

acknowledge the DST-FIST program for the Bruker D8 Quest Eco X-ray diffractometer. L.R.D. acknowledges CSIR (Grant No. 01(2923)/18/EMR-II) for the SRF and Goa University for the Research Studentship. Financial assistance to the School of Chemical Sciences (formerly Department of Chemistry), Goa University under the Special Assistance Program (DSA-1) of UGC-India is gratefully acknowledged. The authors acknowledge the Central Instrumentation facility at IISER Bhopal for assisting us with the SQUID-VSM facility. The authors thank Prof. B. R. Srinivasan for his valuable discussions on single-crystal X-ray data and Dr. Venkatesha R. Hathwar for his valuable inputs on the interpretation of simulated and experimental X-ray powder patterns of our compounds.

REFERENCES

(1) Batten, S. R.; Champness, N. R.; Chen, X.-M.; Garcia-Martinez, J.; Kitagawa, S.; Ohrstom, L.; O'Keeffe, M.; Paik Suh, M.; Reedijk, J. Terminology of Metal-Organic Frameworks and Coordination Polymers (IUPAC Recommendations 2013). *Pure Appl. Chem.* **2013**, *85*, 1715−1724.

(2) Batten, S. R.; Neville, S. M.; Turner, D. R. *Coordination Polymers: Design, Analysis, and Application*; RSC Publication, 2009; pp 1−18.

(3) Long, J. R.; Yaghi, O. M. The Pervasive Chemistry of Metal-Organic Frameworks. *Chem. Soc. Rev.* **2009**, *38*, 1213−1214.

(4) Janiak, C. Engineering Coordination Polymers towards Applications. *Dalton Trans.* **2003**, *3*, 2781−2804.

(5) Stock, N.; Biswas, S. Synthesis of Metal-Organic Frameworks (MOFs): Routes to Various MOF Topologies, Morphologies, and Composites. *Chem. Rev.* **2012**, *112*, 933−969.

(6) Kitagawa, S.; Kitaura, R.; Noro, S. I. Functional Porous Coordination Polymers. *Angew. Chem., Int. Ed.* **2004**, *43*, 2334−2375.

(7) Yaghi, O. M.; O'Keeffe, M.; Ockwig, N. W.; Chae, H. K.; Eddaoudi, M.; Kim, J. Reticular Synthesis and the Design of New Materials. *Nature* **2003**, *423*, 705−714.

(8) Duangthongyou, T.; Jirakulpattana, S.; Phakawatchai, C.; Kurmoo, M.; Siripaisarnpipat, S. Comparison of Crystal Structures and Magnetic Properties of Two Co(II) Complexes Containing Different Dicarboxylic Acid Ligands. *Polyhedron* **2010**, *29*, 1156−1162.

(9) Tranchemontagne, D. J.; Mendoza-Cortés, J. L.; O'Keeffe, M.; Yaghi, O. M. Secondary Building Units, Nets and Bonding in the Chemistry of Metal-Organic Frameworks. *Chem. Soc. Rev.* **2009**, *38*, 1257−1283.

(10) Burgoyne, A. R.; Meijboom, R. Knoevenagel Condensation Reactions Catalysed by Metal-Organic Frameworks. *Catal. Lett.* **2013**, *143*, 563−571.

(11) Zhu, L.; Liu, X. Q.; Jiang, H. L.; Sun, L. B. Metal-Organic Frameworks for Heterogeneous Basic Catalysis. *Chem. Rev.* **2017**, *117*, 8129−8176.

(12) Remya, V. R.; Kurian, M. Synthesis and Catalytic Applications of Metal-organic Frameworks: A Review on Recent Literature. *Int. Nano Lett.* **2019**, *9*, 17−29.

(13) Hou, Y.-X.; Sun, J.-S.; Zhang, D.-P.; Qi, D.-D.; Jiang, J.-Z. Porphyrin-Alkaline Earth MOFs with the Highest Adsorption Capacity for Methylene Blue. *Chem. - Eur. J.* **2016**, *22*, 6345−6352.

(14) Gaur, R. Selective Anionic Dye Adsorption, Topology, and Luminescence Study of Structurally Diverse Cadmium(II) Coordination Polymers. *Inorg. Chem. Front.* **2019**, *6*, 278−286.

(15) Li, J.-R.; Kuppler, R. J.; Zhou, H.-C. Selective Gas Adsorption and Separation in Metal-Organic Frameworks. *Chem. Soc. Rev.* **2009**, *38*, 1477−1504.

(16) Barea, E.; Montoro, C.; Navarro, J. A. R. Toxic Gas Removal-Metal-Organic Frameworks for the Capture and Degradation of Toxic Gases and Vapours. *Chem. Soc. Rev.* **2014**, *43*, 5419−5430.

(17) Datta, A.; Das, K.; Massera, C.; Clegg, J. K.; Pfrunder, M. C.; Garribba, E.; Huang, J.-H.; Sinha, C.; Maji, T. K.; Akitsu, T.; Orita, S. A 2-D Coordination Polymer Incorporating Cobalt(II), 2-Sulfoterephthalate and the Flexible Bridging Ligand 1,3-Di(4-pyridyl)-propane. *Inorg. Chem. Front.* **2015**, *2*, 157−163.

(18) Halder, A.; Bhattacharya, B.; Haque, F.; Ghoshal, D. Structural Diversity in Six Mixed Ligand Zn(II) Metal-Organic Frameworks Constructed by Rigid and Flexible Dicarboxylates and Different N, N′ Donor Ligands. *Cryst. Growth Des.* **2017**, *17*, 6613−6624.

(19) Maji, T. K.; Matsuda, R.; Kitagawa, S. A Flexible Interpenetrating Coordination Framework with a Bimodal Porous Functionality. *Nat. Mater.* **2007**, *6*, 142−148.

(20) Lama, P.; Mrozinski, J.; Bharadwaj, P. K. Co(II) Coordination Polymers with Co-Ligand Dependent Dinuclear to Tetranuclear Core: Spin-Canting, Weak Ferromagnetic, and Antiferromagnetic Behavior. *Cryst. Growth Des.* **2012**, *12*, 3158−3168.

(21) Lee, E. W.; Kim, Y. J.; Jung, D.-Y. A Coordination Polymer of Cobalt(II)-Glutarate Two-Dimensional Interlocking Structure by Dicarboxylate Ligands with Two Different Conformations. *Inorg. Chem.* **2002**, *41*, 501−506.

(22) Bhattacharya, B.; Maity, D. K.; Pachfule, P.; Colacio, E.; Ghoshal, D. Syntheses, X-ray Structures, Catalytic Activity and Magnetic Properties of Two New Coordination Polymers of Co(II) and Ni(II) Based on Benzenedi-carboxylate and Linear N, N′-Donor Schiff Base Linker. *Inorg. Chem. Front.* **2014**, *1*, 414−425.

(23) Liu, T.; Chen, Y.-H.; Zhang, Y.-J.; Wang, Z.-M.; Gao, S. NaCl-Type Frameworks of $[M(pyrazine)_2NO_2]ClO_4$ (M = Co, Cu), The First Examples Containing $\mu_{1,3}$- Nitrito Bridges Showing Antiferromagnetism. *Inorg. Chem.* **2006**, *45*, 9148−9150.

(24) Chao, T.-L.; Yang, C.-I. Three New Homochiral Coordination Polymers Involving Two Three-Dimensional Structural Architectures: Syntheses, Structures, and Magnetic Properties. *J. Solid State Chem.* **2014**, *211*, 25−31.

(25) Abbasi, A.; Tarighi, S.; Badiei, A. A Three-dimensional Highly Stable Cobalt(II) Metal-Organic Framework Based on Terephthalic Acid: Synthesis, Crystal Structure, Thermal and Physical Properties. *Transition Met. Chem.* **2012**, *37*, 679−685.

(26) Seetharaj, R.; Vandana, P. V.; Arya, P.; Mathew, S. Dependence of Solvents, pH, Molar Ratio and Temperature in Tuning Metal-Organic Framework Architecture. *Arabian J. Chem.* **2019**, *12*, 295−315.

(27) Forster, P. M.; Burbank, A. R.; Livage, C.; Férey, G.; Cheetham, A. K. The Role of Temperature in the Synthesis of Hybrid Inorganic-organic Materials: The Example of Cobalt Succinates. *Chem. Commun.* **2004**, *38*, 368−369.

(28) Livage, C.; Egger, C.; Férey, G. Hydrothermal versus Non-hydrothermal Synthesis for the Preparation of Organic-Inorganic Solids: The Example of Cobalt(II) Succinate. *Chem. Mater.* **2001**, *13*, 410−414.

(29) Forster, P. M.; Stock, N.; Cheetham, A. K. A High-Throughput Investigation of the Role of pH, Temperature, Concentration, and Time on the Synthesis of Hybrid Inorganic-Organic Materials. *Angew. Chem., Int. Ed.* **2005**, *44*, 7608−7611.

(30) Forster, P. M.; Burbank, A. R.; O'Sullivan, M. C.; Guillou, N.; Livage, C.; Férey, G.; Stock, N.; Cheetham, A. K. Single-Crystal Characterization of $Co_7(OH)_6(H_2O)_3.(C_4H_4O_4)_4{\cdot}7H_2O$; A New Cobalt Succinate Identified through High-Throughput Synthesis. *Solid State Sci.* **2005**, *7*, 1549−1555.

(31) Nagarkar, S. S.; Joarder, B.; Chaudhari, A. K.; Mukherjee, S.; Ghosh, S. K. Highly Selective Detection of Nitro Explosives by a Luminescent Metal-Organic Framework. *Angew. Chem., Int. Ed.* **2013**, *52*, 2881−2885.

(32) Nagarkar, S. S.; Desai, A. V.; Ghosh, S. K. Engineering Metal-Organic Frameworks for Aqueous Phase 2,4,6-Trinitrophenol (TNP) Sensing. *CrystEngComm* **2016**, *18*, 2994−3007.

(33) Xu, H.; Liu, F.; Cui, Y.; Chen, B.; Qian, G. A Luminescent Nanoscale Metal-Organic Framework for Sensing of Nitroaromatic Explosives. *Chem. Commun.* **2011**, *47*, 3153−3155.

(34) Lakowicz, J. R. *Principles of Fluorescence Spectroscopy*; Springer, MA Publication, 2006.

https://doi.org/10.1021/acsomega.1c05216
ACS Omega 2022, 7, 5698−5712

(35) Li, Y.-L.; Zhao, Y.; Wang, P.; Kang, Y.-S.; Liu, Q.; Zhang, X.-D.; Sun, W.-Y. Multifunctional Metal-Organic Frameworks with Fluorescent Sensing and Selective Adsorption Properties. *Inorg. Chem.* **2016**, *55*, 11821−11830.
(36) Lan, A.-J.; Li, K.-H.; Wu, H.-H.; Olson, D. H.; Emge, T. J.; Ki, W.; Hong, M.-C.; Li, J. A Luminescent Microporous Metal-Organic Framework for the Fast and Reversible Detection of High Explosives. *Angew. Chem., Int. Ed.* **2009**, *48*, 2334−2338.
(37) Gogia, A.; Mandal, S. K. A Rational Design and Green Synthesis of 3D Metal-Organic Frameworks Containing a Rigid Heterocyclic Nitrogen-rich Dicarboxylate: Structural Diversity, CO_2 Sorption and Selective Sensing of 2, 4, 6- TNP in Water. *Dalton Trans.* **2019**, *48*, 2388−2398.
(38) Mao, H.; Wang, E.; Zhang, C.; Li, G.; Zhang, H.; Hou, H.; Li, L.; Wu, Q.; Zhu, Y. New Types of the Flexible Self-Assembled Metal-Organic Coordination Polymers Constructed by Aliphatic Dicarboxylates and Rigid Bidentate Nitrogen Ligands. *Dalton Trans.* **2004**, 3918−3925.
(39) Sahoo, M. K.; Samantara, A. K.; Behera, J. N. In Situ Transformed Cobalt Metal-Organic Framework Electrocatalysts for the Electrochemical Oxygen Evolution Reaction. *Inorg. Chem.* **2020**, *59*, 12252−12262.
(40) Zheng, Y.-Q.; Lin, J.-L. Crystal Structure of *catena*-tetraaquasuccinato-*O,O′*-cobalt(II), $Co(C_4H_4O_4)(H_2O)_4$. *Z. Kristallogr.* **2000**, *215*, 159−160.
(41) Sheldrick, G. M. Crystal Structure Refinement with SHELXL. *Acta Crystallogr., Sect. C: Struct. Chem.* **2015**, *71*, 3−8.
(42) de Campos, E. A.; Silva, N. J. O.; Shi, F.-N.; Rocha, J. Cobalt(II)−pyrazine−chloride Coordination Polymers: Synthesis, Reactivity, and Magnetic Properties. *CrystEngComm* **2014**, *16*, 10439−10444.
(43) Nadeem, M. A.; Bhadbhade, M.; Bircher, R.; Stride, J. A. Controlled Synthesis of Isomorphous Coordination Polymers via in Situ Ligand Transformation Reaction: Crystal Structure, Thermal, and Magnetic Properties. *Cryst. Growth Des.* **2010**, *10*, 4060−4067.
(44) James, M. The Structure and Magnetic Properties of the Two-Dimensional Dipyrazine-Bridged Polymers $M(pz)_2Br_2$ (M = Fe^{II}, Co^{II}, Ni^{II}). *Aust. J. Chem.* **2002**, *55*, 219−223.
(45) Zhang, K.-L.; Wang, Z.; Huang, H.; Zhu, Y.; You, X.-Z. Synthesis, Crystal Structure, and Magnetic Properties of a Novel Dinuclear Cobalt(II) Complex Based on the Mixed N and O- Donor Ligands: $[Co_2(pyrazine)(fumarato)_2(H_2O)_8]\cdot 7H_2O$. *J. Mol. Struct.* **2004**, *693*, 193−197.
(46) Delgado, F. S.; Sanchiz, J.; Ruiz-Pérez, C.; Lloret, F.; Julve, M. High-Dimensional Malonate-Based Materials: Synthesis, Crystal Structures, and Magnetic Properties of $[M_2(mal)_2(L)(H_2O)_2]_n\cdot n(H_2O)$ M = Zn (II), Co (II); H_2 mal = Malonic Acid, L= Pyrimidine, Pyrazine. *CrystEngComm* **2003**, *5*, 280−284.
(47) Smith, M. B.; March, J. *March's Advanced Organic Chemistry: Reactions, Mechanisms and Structure*, 6th ed.; John Wiley & Sons: New Jersey, 2007; pp 136−233.
(48) Roy, S.; Choubey, S.; Khan, S.; Bhar, K.; Ribas, J.; Ghosh, B. K. Synthesis, Characterization and Magnetic Property of a Succinate Bridged 1D Coordination Polymer of Cobalt(II) Containing Benzidine as End-Capping Ligand. *J. Mol. Struct.* **2014**, *1061*, 54−60.
(49) Sokolow, J. D.; Trzop, E.; Chen, Y.; Tang, J.; Allen, L. J.; Crabtree, R. H.; Benedict, J. B.; Coppens, P. Binding Modes of Carboxylate and Acetylacetonate Linked Chromophores to Homodisperse Polyoxotitanate Nanoclusters. *J. Am. Chem. Soc.* **2012**, *134*, 11695−11700.
(50) Duangthongyou, T.; Phakawatchai, C.; Siripaisarnpipat, S. Synthesis and Fluorescence of Multi-Dimensional Structures of Two Cobalt (II) Complexes between 2,2′-Bipyridine and Different Chain Length of Aliphatic Dicarboxylic, Succinic or Glutaric Acid. *J. Mol. Struct.* **2011**, *987*, 101−105.
(51) Gong, Y.; Hu, C.; Li, H.; Tang, W. Two Novel Coordination Polymers with Different Molecular Tectonics based on Cobalt−Succinate-Organoamine Systems. *Inorg. Chem. Commun.* **2006**, *9*, 273−276.
(52) Zheng, Y.-Q.; Kong, Z.-P. Crystal Structure of Mono Aqua(1,10-phenanthroline-N, N′)-Succinatocobalt(II), $Co(H_2O)(C_{12}H_8N_2)(C_4H_4O_4)$. *Z. Kristallogr. - New Cryst. Struct.* **2003**, *218*, 223−224.
(53) Demir, S.; Kantar, G. K.; Topcu, Y.; Li, Q. Solvothermal Synthesis and Characterization of Coordination Polymers of Cobalt-(II) and Zinc(II) with Succinic Acid. *Transition Met. Chem.* **2012**, *37*, 257−263.
(54) Filippova, I. G.; Malaestean, I. L.; Baca, S. G. Synthesis and Crystal Structures of Manganese(II) and Cobalt(II) Complexes with 2, 6-Dimethoxybenzoic Acid and Additional N-donor Ligands. *Z. Anorg. Allg. Chem.* **2014**, *640*, 31−34.
(55) Blatov, V. A.; O' Keeffe, M.; Proserpio, D. M. Vertex-, face-, point-, Schläfli-, and Delaney- Symbols in Nets, Polyhedra and Tilings: Recommended Terminology. *CrystEngComm* **2010**, *12*, 44−48.
(56) Mitina, T. G.; Blatov, V. A. Topology of 2-Periodic Coordination Networks: Toward Expert Systems in Crystal Design. *Cryst. Growth Des.* **2013**, *13*, 1655−1664.
(57) Serezhkin, V. N.; Vologzhanina, A. V.; Serezhkina, L. B.; Smirnova, E. S.; Grachova, E. V.; Ostrova, P. V.; Antipin, M. Y. Crystallochemical Formula as a Tool for Describing Metal-Ligand Complexes - a Pyridine-2,6-Dicarboxylate Example. *Acta Crystallogr., Sect. B: Struct. Sci.* **2009**, *65*, 45−53.
(58) Sokolov, A. V.; Vologzhanina, A. V.; Barabanova, E. D.; Stefanovich, S. Y.; Dorovatovskii, P. V.; Taydakov, I. V.; Alexandrov, E. V. Coordination Properties of Hydroxyisophthalic Acids: Topological Correlations, Synthesis, Structural Analysis, and Properties of New Complexes. *Chem. - Eur. J.* **2021**, *27*, 9180−9192.
(59) Shevchenko, A. P.; Alexandrov, E. V.; Golov, A. A.; Blatova, O. A.; Duyunova, A. S.; Blatov, V. A. Topology Versus Porosity: What can Reticular Chemistry Tell us About Free Space in Metal−Organic Frameworks? *Chem. Commun.* **2020**, *56*, 9616−9619.
(60) Yang, S.-Y.; Long, L.-S.; Huang, R.-B.; Zheng, L.-S.; Ng, S. K. Catena Poly[[[tetraaquacobalt(II)]-μ-pyrazine] phthalate]. *Acta Crystallogr., Sect. E: Struct. Rep. Online* **2003**, *59*, m961−m963.
(61) Holman, K. T.; Hammud, H. H.; Isber, S.; Tabbal, M. One-Dimensional Coordination Polymer $[Co(H_2O)_4(pyz)](NO_3)_2\cdot 2H_2O$ (pyz = pyrazine) with Intra- and Inter-Chain H-bonds: Structure, Electronic Spectral Studies, and Magnetic Properties. *Polyhedron* **2005**, *24*, 221−228.
(62) Fetzer, Th.; Jooss, R.; Lentz, A.; Debaerdernaeker, T. Crystal Growth, and Structure of $CoSO_4\cdot$ Pyrazine $\cdot 6H_2O$ (I) and $(CoSO_4)\cdot$ Pyrazine $\cdot 12H_2O$ (II). *Z. Anorg. Allg. Chem.* **1994**, *620*, 1750−1754.
(63) Lu, J.; Paliwala, T.; Lim, S. C.; Yu, C.; Niu, T.; Jacobson, A. J. Coordination Polymers of $Co(NCS)_2$ with Pyrazine and 4,4′-Bipyridine: Syntheses and Structures. *Inorg. Chem.* **1997**, *36*, 923−929.
(64) Wriedt, M.; Jess, I.; Näther, C. Poly[bis(cyanato-κN)bis(μ-pyrazine- κ^2N: N′)cobalt(II)]. *Acta Crystallogr., Sect. E: Struct. Rep. Online* **2009**, *65*, m431.
(65) Wriedt, M.; Näther, C. Synthesis, Crystal Structures, Thermal and Magnetic Properties of New Selenocyanato Coordination Polymers with Pyrazine as Co-Ligand. *Z. Anorg. Allg. Chem.* **2011**, *637*, 666−671.
(66) Alexandrov, E. V.; Virovets, A. V.; Blatov, V. A.; Peresypkina, E. V. Topological Motifs in Cyanometallates: From Building Units to Three-Periodic Frameworks. *Chem. Rev.* **2015**, *115*, 12286−12319.
(67) Zheng, Y.-Q.; Lin, J.-L. Crystal Structure of *catena*-tetraaquasuccinato-*O,O′*-nickel(II), $Ni(C_4H_4O_4)(H_2O)_4$. *Z. Kristallogr. - New Cryst. Struct.* **2000**, *215*, 157−158.
(68) Xu, T.-G.; Xu, D.-J.; Wu, J.-Y.; Chiang, M. Y. *catena*-Poly[[tetraaquairon(II)]-μ-succinato-κ^2O:O']. *Acta Crystallogr., Sect. C: Cryst. Struct. Commun.* **2002**, *58*, m615−m616.
(69) Baier, J.; Thewal, U. Representation and Structures of Mg Complexes with α, ω-Dicarboxylato Ligands (dicarboxylate = succinate, glutarate and suberate). *Z. Anorg. Allg. Chem.* **2002**, *628*, 315−321.

https://doi.org/10.1021/acsomega.1c05216
ACS Omega 2022, 7, 5698−5712

(70) Fleck, M.; Tillmanns, E.; Bohaty, L. Crystal Structure of Tetraaquamanganese Succinate, $Mn(H_2O)_4C_4H_4O_4$. *Z. Kristallogr. - New Cryst. Struct.* **2000**, *215*, 429−430.
(71) Roy, S.; Choubey, S.; Khan, S.; Bhar, K.; Ribas, J.; Ghosh, B. K. Synthesis, Characterization and Magnetic Property of a Succinate Bridged 1D Coordination Polymer of Cobalt(II) Containing Benzidine as End-Capping Ligand. *J. Mol. Struct.* **2014**, *1061*, 54−60.
(72) Calderone, P. J.; Banerjee, D.; Plonka, A. M.; Kim, S. J.; Parise, J. B. Temperature-Dependent Structure Formation and Photoluminescence Studies of a Series of Magnesium-Based Coordination Networks. *Inorg. Chim. Acta* **2013**, *394*, 452−458.
(73) Li, C.-P.; Du, M. Role of Solvents in Coordination Supramolecular Systems. *Chem. Commun.* **2011**, *47*, 5958−5972.
(74) Kaufman, A.; Afshar, C.; Rossi, M.; Zacharias, D. E.; Glusker, J. P. Metal Ion Coordination in Cobalt Formate Dihydrate. *Struct. Chem.* **1993**, *4*, 191−198.
(75) Burlet, P.; Rossat-Mignod, J.; Matsuura, M. Magnetic Structure of Cobalt Formate Dihydrate: a Single Crystal Determination. *J. Phys., Lett.* **1979**, *40*, 455−457.
(76) Zhao, J.-P.; Han, S.-D.; Zhao, R.; Yang, Q.; Chang, Z.; Bu, X.-H. Tuning the Structure and Magnetism of Heterometallic Sodium-(1+) - Cobalt(2+) Formate Coordination Polymers by Varying the Metal Ratio and Solvents. *Inorg. Chem.* **2013**, *52*, 2862−2869.
(77) Wang, X-Y.; Gan, L.; Zhang, S.-W.; Gao, S. Perovskite-like Metal Formates with Weak Ferromagnetism and as Precursors to Amorphous Materials. *Inorg. Chem.* **2004**, *43*, 4615−4625.
(78) Jing, S.; Xu, J.-N.; Song, T.-Y.; Xin, H.; Ye, J.-W.; Wang, L.; Yang, F.; Zhang, P. Hydrothermal Synthesis and Structure of $[Co(imi)_6]\cdot(NBA)_2\cdot 2H_2O$ (imi = imidazole, NBA = 4-nitrobenzoic acid). *J. Coord. Chem.* **2007**, *60*, 295−300.
(79) Nakamoto, K. *Infrared and Raman Spectra of Inorganic and Coordination Compounds Part A: Theory and Applications in Inorganic Chemistry*, 6th ed.; John Wiley: New York, 2009; pp 149−354.
(80) Suzuki, M.; Shimanouchi, T. Infrared and Raman Spectra of Succinic Acid Crystal. *J. Mol. Spectrosc.* **1968**, *28*, 394−410.
(81) Simmons, J. D.; Innes, K. K.; Begun, G. M. Infrared and Raman spectra of pyrazine-h4 and -d4. *J. Mol. Spectrosc.* **1964**, *14*, 190−197.
(82) Demir, S.; Yilmaz, V. T.; Yilmaz, F.; Buyukgungor, O. One-Dimensional Cobalt(II) and Zinc(II) Succinato Coordination Polymers with Nicotinamide: Synthesis, Structural, Spectroscopic, Fluorescent, and Thermal Properties. *J. Inorg. Organomet. Polym.* **2009**, *19*, 342−347.
(83) Jin, J.; Gong, Y.; Li, L.; Han, X.; Meng, Q.; Liu, Y.; Niu, S. Spectroscopic Properties of a Series of Co(II) Coordination Polymers and the Influence of Co(II) Coordination Environment on Photoelectric Property. *Spectrochim. Acta, Part A* **2015**, *137*, 856−863.
(84) Macrae, C. F.; Sovago, I.; Cottrell, S. J.; Galek, P. T. A.; McCabe, P.; Pidcock, E.; Platings, M.; Shields, G. P.; Stevens, J. S.; Towler, M.; Wood, P. A. Mercury 4.0: From Visualization to Analysis, Design and Prediction. *J. Appl. Crystallogr.* **2020**, *53*, 226−235.
(85) Shi, L.; Shao, D.; Wei, H.-Y.; Wang, X.-Y. Two Interpenetrated Cobalt(II) Metal−Organic Frameworks with Guest-Dependent Structures and Field-Induced Single-Ion Magnet Behaviors. *Cryst. Growth Des.* **2018**, *18*, 5270−5278.
(86) Kawade, V. A.; Bhat, S. S.; Tayade, S. B.; Kumbhar, A. S. A One-Dimensional Self-Assembled Porous Coordination Polymer Poly[bis(picolinato-N,O)(μ-1,2-bis(4 pyridyl)ethane-N, N′)cobalt-(II)] Dimethanol. *Inorg. Chim. Acta* **2018**, *483*, 539−543.
(87) Hwang, I. H.; Bae, J. M.; Kim, W.-S.; Jo, Y. D.; Kim, C.; Kim, Y.; Kim, S.-J.; Huh, S. Bifunctional 3D Cu-MOFs Containing Glutarates and Bipyridyl Ligands: Selective CO_2 Sorption and Heterogeneous Catalysis. *Dalton Trans.* **2012**, *41*, 12759−12765.
(88) Thommes, M.; Kaneko, K.; Neimark, A. V.; Olivier, J. P.; Rodriguez-Reinoso, F.; Rouquerol, J.; Sing, K. S. W. Physisorption of Gases, with Special Reference to the Evaluation of Surface Area and Pore Size Distribution (IUPAC Technical Report). *Pure Appl. Chem.* **2015**, *87*, 1051−1069.
(89) Le-Bail, A.; Duroy, H.; Fourquet, J. L. Ab-initio Structure Determination of $LiSbWO_6$ by X-ray Powder Diffraction. *MRS Bull.* **1988**, *23*, 447−452.
(90) Le-Bail, A. Whole Powder Pattern Decomposition Methods and Applications: A Retrospection. *Powder Diffr.* **2005**, *20*, 316−326.
(91) Wang, G.-Y.; Yang, L.-L.; Li, Y.; Song, H.; Ruan, W.-J.; Chang, Z.; Bu, X.-H. A Luminescent 2D Coordination Polymer for Selective Sensing of Nitrobenzene. *Dalton Trans.* **2013**, *42*, 12865−12868.
(92) Gao, Q.; Xu, J.; Bu, X.-H. Recent Advances About Metal−Organic Frameworks in the Removal of Pollutants from Waste Water. *Coord. Chem. Rev.* **2019**, *378*, 17−31.
(93) Harmalkar, S. S.; Naik, A. V.; Nilajakar, M. K.; Dhuri, S. N. Chemoselective Detection of 2,4,6-Trinitrophenol by Ground State Adduct Formation via Protonation of Quinoline Moiety of Non-heme Ligands with Structural Evidence. *ChemistrySelect* **2020**, *5*, 8447−8454.
(94) Tian, D.; Li, Y.; Chen, R.-Y.; Chang, Z.; Wang, G.-Y.; Bu, X.-H. A Luminescent Metal-Organic Framework Demonstrating Ideal Detection Ability for Nitroaromatic Explosives. *J. Mater. Chem. A* **2014**, *2*, 1465−1470.
(95) Das, P.; Mandal, S. K. Strategic Design and Functionalization of an Amine-decorated Luminescent Metal-Organic Framework for Selective Gas/Vapor Sorption and Nanomolar Sensing of 2,4,6-Trinitrophenol in Water. *ACS Appl. Mater. Interfaces* **2018**, *10*, 25360−25371.
(96) Gole, B.; Bar, A. K.; Mukherjee, P. S. Fluorescent Metal-Organic Framework for Selective Sensing of Nitroaromatic Explosives. *Chem. Commun.* **2011**, *47*, 12137−12139.
(97) Gole, B.; Song, W.; Lackinger, M.; Mukherjee, P. S. Explosives Sensing by Using Electron-Rich Supramolecular Polymers: Role of Intermolecular Hydrogen Bonding in Significant Enhancement of Sensitivity. *Chem. - Eur. J.* **2014**, *20*, 13662−13680.
(98) Wang, D.; Hu, Z.; Xu, S.; Li, D.; Zhang, Q.; Ma, W.; Zhou, H.; Wu, J.; Tian, Y. Fluorescent Metal-Organic Frameworks Based on Mixed Organic Ligands: New Candidates for Highly Sensitive Detection of TNP. *Dalton Trans.* **2019**, *48*, 1900−1905.
(99) Hinterholzinger, F. M.; Rühle, B.; Wuttke, S.; Karaghiosoff, K.; Bein, T. Highly Sensitive and Selective Fluoride Detection in Water Through Fluorophore Release from a Metal-Organic Framework. *Sci. Rep.* **2013**, *3*, No. 2562.
(100) Rachuri, Y.; Parmar, B.; Suresh, E. Three Dimensional Co(II)/Cd(II) MOFs: Luminescent Cd- MOF for Detection and Adsorption of TNP in Aqueous Phase. *Cryst. Growth Des.* **2018**, *18*, 3062−3072.

https://doi.org/10.1021/acsomega.1c05216
ACS Omega 2022, 7, 5698−5712